A Frequency Reconfigurable Circularly Polarized Microstrip Patch Antenna Using Liquid Metal Microswitches

by

Steven Christopher Yee

B.S. Electrical Engineering
United States Naval Academy, 2011

Submitted to the
Department of Electrical Engineering and Computer Science
in partial fulfillment of the requirements for the degree of

Master of Science in Electrical Engineering
at the
Massachusetts Institute of Technology

June 2013

Author.....
Department of Electrical Engineering
May 10, 2013

Certified by.....
Amy Duwel, Ph.D.
Charles Stark Draper Laboratory
Thesis Supervisor

Certified by.....
Dana Weinstein
Assistant Professor of Electrical Engineering
Thesis Advisor

Accepted by.....
Leslie Kolodziejski
Chair, Department Committee on Graduate Students
Professor of Electrical Engineering

A Frequency Reconfigurable Circularly Polarized Microstrip Patch Antenna Using Liquid Metal Microswitches

by

Steven Christopher Yee

Submitted to the
Department of Electrical Engineering and Computer Science
on 10 May 2013 in partial fulfillment of the requirements for the
degree of Master of Science in Electrical Engineering

Abstract

Reconfigurable antennas with adaptable frequency, pattern, and polarization offer flexibility and size reduction for wireless systems that must increasingly execute multiple missions with less volume. These antennas will also complement anticipated cognitive radio systems, which promise more efficient use of the electromagnetic spectrum. Microscale liquid metal switches are proposed to overcome the series loss, mechanical fatigue, and limited power handling reliability of common methods of antenna reconfiguration such as semiconductor diodes and microelectromechanical switches. The proposed microswitches consist of mercury droplets that selectively connect solid metal traces.

Both fluidic and electrostatic switch actuation mechanisms are investigated, and an electrostatic switch is demonstrated. Electrostatically actuated switches are designed into a compact single-feed patch antenna configurable between two communication frequency bands and a GPS band with different circular polarizations. The antenna topology is based on a corner truncated square patch with switched sets of extensions to achieve resonant frequency and axial ratio control. Measurements of reconfigurable prototypes demonstrate frequency and polarization configurability in good agreement with full-wave simulations. The proposed reconfiguration mechanism is compared to other methods, and future directions for the integration of microfluidics in reconfigurable radio frequency systems are proposed.

Thesis Supervisor: Amy Duwel
Title: RF and Communications Group Leader, Charles Stark Draper Laboratory

Thesis Advisor: Dana Weinstein
Title: Assistant Professor of Electrical Engineering

Acknowledgements

Many engineers and lab technicians at Draper have assisted me in all manner of processes during my research odyssey these past two years. Although not all the work that they assisted is presented here, they are deeply appreciated contributors to my education. Thanks to Maria Cardoso, Seth Davis, Daniel Frigon, James Hsiao, Joseph Louis, Jim Mahoney, Carlos Martinez, and Jeff Thompson.

This research is an extension of the work begun by the LiquidRF team at Draper. I am indebted to them for laying the groundwork research that greatly simplified material selection and process design. Thank you, Pierre Dufilie, Reed Irion, Jason Fiering, Erin Pararas, and Doug White, for allowing me to join your team and learn from the best. I hope you find the completed reconfigurable prototypes a satisfying manifestation of your original vision. Special thanks goes to Jason Fiering for allowing me to consult him again and again over the course of this research – even after the LiquidRF project officially ended.

Deep gratitude goes to Dave Stone, who not only made many of the prototypes, but also wrestled unruly milling machines and anechoic chamber software into submission for me. Special thanks also belong to Mike Abban, whose suggestion that I retry my electrostatic actuation experiments with silicone oil ended a three-month long struggle that almost derailed the project.

Thanks to the MTL computation team for maintaining the CAD programs used for simulation and handling the office moves and their accompanied complications.

I feel extraordinarily blessed to have had Dr. Amy Duwel as my supervisor and even more blessed to count her as a friend. Her openness to my optimistic visions and sage wisdom when those visions encountered obstacles was everything you could ask of a research mentor. I also thank my advisor, Professor Dana Weinstein, whose work ethic and rigorous thinking has been a source of inspiration. Her broad interests and diverse student group has truly widened my horizons.

Lastly, I extend my heartfelt thanks to my family and especially to my wife, Margaret, whose love and patience I rely on every day.

This thesis was prepared at the Charles Stark Draper Laboratory, Inc., under internal research and development.

Contents

Chapter 1

Introduction

(a) (b) (c)

Figure 1.1: Cellular phones circa (a) 1985, (b) 2002, and (c) 2010.

1.1 Motivation

Recent interest in reconfigurable antennas is a response to the multifunctionality, bandwidth, and hardware turnover problems posed by the continued rapid growth of both wireless technologies and public enthusiasm for them. Demand for ever more capable yet portable phones, tablets, and laptops has put pressure on engineers to incorporate an increasing number of radio technologies into ever shrinking form factors. Smartphones sporting not only cellular service, but also Wi-Fi, Bluetooth, Zigbee, and GPS capabilities are increasingly the norm and not the exception [1]. Meanwhile, the area allotted to antennas continues to shrink.

As wireless devices become both smaller and more multifunctional, their antenna systems must do the same. Frequency reconfigurable antennas offer space efficient solutions to the multifunctionality challenge. A single antenna that can be reconfigured to operate at multiple bands can serve the function of multiple antennas but with a much smaller

footprint. Polarization reconfigurable antennas also present potential for performance enhancement when different wireless technologies use dissimilar polarizations [2].

A second challenge facing the wireless world is the crowding of the electromagnetic spectrum. The spectrum is currently regulated with a static allocation method, limiting legal use of a given bandwidth to only one licensed user ever. The sheer volume of mobile data in the United States is fast approaching the throughput limits of the bandwidth allocated to it [3]. Without a paradigm shift in spectrum regulation, this inefficiency will effectively exhaust a finite resource despite the fact that less than 14% of the spectrum is actually busy at any given moment [4].

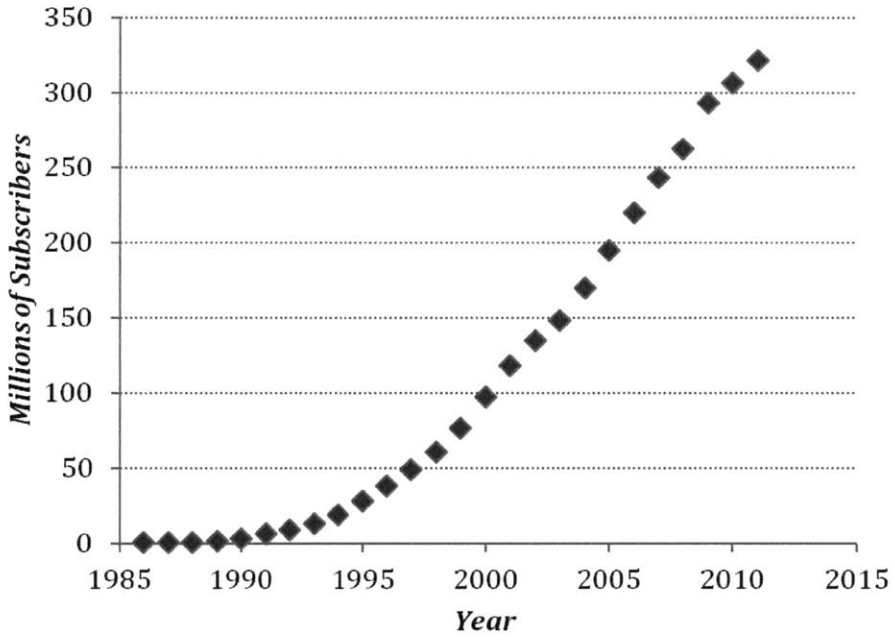

Figure 1.2: Mobile wireless subscriptions in the United States [5].

One promising solution to this problem is cognitive radio, a system in which intelligent radios sense and adapt to their local wireless environment to access more bandwidth and yet avoid interference and wireless chaos. For example, if a local television frequency goes unused at night, nearby cognitive radios would identify and use that frequency until the station begins broadcasting again in the morning [4]. Frequency reconfigurable antennas complement this efficient system by providing smaller and more flexible front ends than those represented by the multiple antennas or large frequency independent antennas required without reconfiguration. Pattern and polarization reconfigurable antennas may also find interference rejection applications in cognitive radio environments by null steering or by operating at controllable cross-polarization to interfering signals [6].

The rapid pace of wireless technology also presents issues of hardware turnover. When one technology is replaced by or must incorporate another, fixed hardware such as conventional antennas becomes obsolete [7]. This issue is especially evident in military systems where updated technology is of critical importance and replacement comes at considerable cost. Although the flexibility of reconfigurable software-defined radios can alleviate the hardware turnover problem, equally flexible antenna technology is required if these systems are to realize their full potential. This is especially true when the system involves antenna arrays such as those commonly used in radar and tracking applications.

Planar antennas, particularly miniaturized dipoles and microstrip patches, have been the focus of most reconfigurable antenna research because their small form factors complement the desired advantages of reconfigurable radio systems. Patch antennas in particular are useful when a low profile and directional gain pattern are desired. Patches have been used in satellite, cellular, Wi-Fi, and radar applications [8]. Geometrical alteration of these antennas through switches is one of the most common methods for reconfiguration. The method has potential to achieve wide frequency, polarization, and pattern shifts. However, traditional switch implementations such as PIN diodes and radio frequency microelectromechanical systems (RF MEMS) have significant disadvantages including high series resistance and poor power handling capability [9].

Liquid metal microfluidic switch technology has the potential to avoid many of the disadvantages associated with typical switch implementations. Linearity, low resistance, and low mechanical wear are just some of the advantages of liquid metals as switch elements in reconfigurable antenna applications. In general, the integration of microfluidic and RF technology presents exciting opportunities for flexible reconfigurable devices.

1.2 Thesis Outline

This thesis explores the design of liquid metal microswitches for microstrip antenna applications and demonstrates their implementation on a three-band frequency and polarization reconfigurable circularly polarized patch antenna. The antenna is designed for GPS, cellular, and ISM band frequencies and polarizations. Chapter 2 presents an overview of antenna reconfiguration and an introduction to microstrip antenna theory. Chapter 3 introduces designs for a microfluidic liquid metal switch. Fluidic and electrostatic actuation mechanisms are compared, and an electrostatic switch is demonstrated. Chapter 4 explores the design of a reconfigurable, circularly polarized three-band microstrip antenna implementing the aforementioned switches. Measured results confirm frequency and polarization configurability in good agreement with full wave simulations. Lastly, Chapter 5 discusses the implications of this work, suggests related future work, and concludes with directions for further integration of microfluidics in reconfigurable RF systems.

Chapter 2

Background

2.1 Overview of Reconfiguration Methods

All antennas are fundamentally passive devices defined by a specified arrangement of conducting and non-conducting elements. Therefore, the possible mechanisms for reconfiguring antennas can be summarized into three categories: those that change the geometry of the elements, those that change the electrical properties of the elements, and those that electrically load the elements with tunable components. Often, the last method can be viewed as a form of geometrical alteration of the antenna. Examples of geometry-based reconfiguration include antennas rotated by motors or selectively connected to other elements by various switches. Ferroelectric materials with controllable permittivity are the basis for most material-based reconfiguration schemes. Varactor diodes or RF MEMS capacitors are common examples of electric loading components [2]. The challenge is to achieve reconfigurability at acceptable costs to performance, size, and complexity.

Of the three general mechanisms for antenna reconfiguration, geometrical alteration offers the most potential for wide frequency, pattern, and polarization shifts because the degrees of freedom in an antenna are limited only by the number of geometrical parameters. By contrast, tunable materials and electrical components are typically constrained to variations in permittivity, permeability, capacitance, or inductance over very limited tuning ranges. Ferroelectric and ferrite materials also suffer from high magnetic losses. Tunable reactive components such as RF MEMS and diode varactors can undesirably change antenna radiation patterns when they significantly alter the topology of current paths on the radiator [2].

Admittedly, geometrical reconfiguration using motors, stretchable materials [10], and even MEMS actuators [11] can be ill-suited to meet form factor requirements of reconfigurable antennas, and all geometry-based reconfiguration is ultimately space-limited. However, for most applications, the flexibility of geometry-based reconfiguration is attractive, a reality reflected by the fact that most reconfigurable antenna research implements some form of switching mechanism. However, significant trade-offs and limitations remain among existing switch technologies. A controllable, low-resistance microswitch that complements antenna architectures represents an unmet need in the field of reconfigurable antennas. The following sections review switch implementations for antenna reconfiguration. A summary of the advantages and disadvantages of various methods is provided in Table 2.1.

Table 2.1: Comparison of switches for reconfigurable antenna applications

Mechanism	Resistance	Switch Speed	Comments
PIN Diodes	~100s of mΩ	~10s of ns	Nonlinear, constant current bias
Photoconductive	~1s of Ω	~1μs	Constant light bias
RF MEMS	~1Ω	~10s of μs	Stiction, self-actuation, mechanical wear, welding
Microfluidic	~10s of mΩ	~1ms	Slow, potential for temporary bias

PIN Diodes

PIN diodes are commonly used as electrically controlled RF switches in a variety of applications including reconfigurable antennas. Featuring a wide intrinsic semiconductor region between highly doped p-type and n-type regions, these diodes exhibit low capacitance when reverse biased and resistance typically on the order of 100mΩ when strongly forward biased [12]. Typical switching speeds are on the order of tens to hundreds of nanoseconds [13]. Although similar in principle to varactor diodes, PIN diodes are normally used as discrete elements and tunable attenuators instead of tunable capacitors.

Advantages of PIN diodes as switch implementations in reconfigurable antennas include high switching speed, low cost, and wide availability of commercial products. However, PIN diodes require current bias to remain in the on-state, resulting in increased power consumption during operation, and the resistance of PIN diodes can significantly deteriorate the efficiency of reconfigurable antennas that require multiple switches. Layout complexity and the potential for parasitic effects are also increased by the biasing requirements for PIN diodes [2].

Like all diodes, PIN diodes also suffer from nonlinearities, specifically gain compression and intermodulation distortion, which become significant at high power levels used in radar or long range transmit applications. These nonlinear effects have been verified in reconfigurable antennas featuring PIN diodes [6], indicating that PIN diodes may have deleterious consequences for overall antenna performance with increasing power level.

Photoconductive Switches

The photoconductive property of semiconductors presents an alternative solid-state switch mechanism that reduces the parasitic issues associated with electrical biasing. Because these switches are actuated by incident light, additional area previously reserved for electrically conductive biasing lines may be available for the radiator. Photoconductive switches are also relatively fast, with typical switching speeds on the order of microseconds [14]. A number of reconfigurable antennas, including patches and dipoles, have been demonstrated using photoconductive switches [15, 16].

However, photoconductive switches still require significant power levels in the form of incident light to remain in the on-state. In [16], more than 20mW of power were required to bias two photoconductive switches enough to achieve the desired frequency change. Moreover, typical photoconductive switches suffer from very high losses. Resistance will slightly decrease with greater optical power, but antenna performance will still be significantly impaired. Insertion loss of the photoconductive switch used in [16] only reached 0.68dB with 200mW input power. At 10mW input power, the insertion loss was as high as 4dB in the 1–3GHz range. In general, solid-state switches achieve low insertion loss only when biasing levels are high, which increases total system power consumption.

RF MEMS Switches

Unlike solid-state switches, RF MEMS switches rely on microscale electromechanical forces to physically displace micromachined conductors to make or break an electrical contact. Although a wide range of topologies and actuation mechanisms have been explored, RF MEMS relays typically feature a conductive cantilever or bridge displaced by an electrostatic field applied from a control electrode. The electrostatic nature of actuation results in low power consumption in both on or off-states, and the switch is ideally linear. Typical resistances for ohmic contact RF MEMS switches are around 1Ω. Insertion losses for capacitive contact RF MEMS switches are typically under 1dB at UHF frequencies. Switching speeds are limited by structural resonances and are normally on the order of tens of microseconds, significantly slower than those of solid-state switches [17]. A growing number of commercial RF MEMS switches are commercially available.

RF MEMS switches suffer from mechanical wear due to structural stresses and their solid-solid contact mechanisms. Although major improvements are being made in RF MEMS reliability, the nature of a solid-solid contact mechanism inevitably limits switch lifetime [1]. RF MEMS switch reliability is also limited by self-actuation and stiction, events in which strong RF signals overwhelm the DC control voltage and cause the MEMS switch to close or remain closed, respectively, regardless of the commanded position [9]. Efforts to avoid stiction and self-actuation issues tend to raise DC control voltage levels. When handling large currents, RF MEMS also may experience welding or arcing phenomena, leading to device failure.

Microfluidic Switches

Liquid metal microfluidic switches can be considered a subclass of MEMS technology, but unlike conventional MEMS switches, microfluidic switches feature fluid-solid or fluid-fluid contacts that avoid mechanical wear. Like their macroscale counterparts, microscale liquid metal switches can provide performance advantages at the cost of switching speed when quality ohmic contacts are required [18]. The fluidic domain also opens up new topology

and actuation possibilities that can reduce self-actuation and stiction issues present in conventional RF MEMS switches. The field of liquid metal microswitches is not yet mature, but it is being researched for a number of applications including reconfigurable antennas.

Mercury and Galinstan are the most commonly used liquid metals featured in liquid metal microswitch research. Galinstan is a proprietary alloy named for the major elements in its composition: gallium, indium, and tin. Unlike mercury, it is not highly toxic and has low surface tension. In fact, Galinstan is three times more conductive than mercury. However, Galinstan easily wets nearly all surfaces and aggressively reacts with metals, limiting its potential in reliable microswitch applications [18]. The toxicity of mercury is a serious concern, but the amounts normally used in microscale devices tend to be far less than the maximum allowed by safety regulations. In fact, microscale mercury devices often contain less mercury than compact fluorescent light bulbs do [19]. Mercury represents a viable option for liquid metal microswitches, although development of unaggressive, non-toxic liquid metal alternatives would be considered more than welcome progress.

Microscale switches using liquid metals have ranged from versions of conventional RF MEMS switches with liquid metal droplets deposited on the contact areas [20, 21] to pressure and electrostatically-driven slugs of liquid metal undergoing large displacements [22, 23]. Reported resistances have ranged from tens of milliohms to about 2 ohms, significantly lower than the range of resistances seen in conventional RF MEMS or solid-state devices [14]. However, typical switching times for liquid metal microswitches are on the order of milliseconds. The fastest reported switching speed for a liquid metal microswitch of 500μs was achieved by electrowetting modulation of droplet contact edges [24]. Although slower than conventional RF MEMS relays and far slower than solid-state switches, microfluidic liquid metal switches may still be advantageous for reconfigurable antenna applications. Reconfigurable antennas have relatively infrequent switching events, and therefore, high conductivity liquid metal switches with speeds on the order of milliseconds may be an acceptable tradeoff.

The vast majority of liquid metal microswitches have not been applied to antenna applications, and those that have tend to omit actuation considerations. A slot antenna using channels of liquid metal to implement switches was made [9], but the design lacks features to control switch state and is manually pumped by a syringe. Another design features a dipole composed entirely of liquid metal with Laplace barriers as a kind of switch to define the antenna length. Fluid pressure is used to break the natural oxide at the surface of the liquid metal, allowing it to move past the Laplace barrier and extend the antenna to the next barrier. However, this method is not reversible [25]. This thesis aims to demonstrate controllable, bistable, low resistance liquid metal microswitches on a frequency and polarization reconfigurable patch antenna.

2.2 Microstrip Patch Antennas

Microstrip antennas are a class of antennas developed in the 1950s as an outgrowth of microstrip transmission line development [8]. Often referred to as patches, these antennas generally consist of a planar conducting radiator parallel to and separated from a ground plane by an electrically small distance. The dielectric between the patch and the ground plane can be air or a circuit board material referred to as the substrate. These antennas typically resonate in a broadside mode with maximum gain normal to the plane of the patch. The patch itself may take a variety of shapes, although rectangular and circular patches are most common due to their ease of analysis. Antenna frequency and pattern are determined by the modes supported by the patch geometry.

Transmission Line Model

Conceptually, a patch antenna operating in a traditional first order mode can be viewed as two radiating apertures separated by a transmission line that is a half wavelength long at the operating frequency. The half wavelength stipulation ensures that the electric fields at the radiating edges are 180° out of phase, which results in far field broadside radiation. Physically, the radiating apertures are two opposite edges of a patch antenna. The length of the patch itself represents the physical length of the transmission line, thus yielding a simple approximate relation between the patch length L and operating frequency f_{100}.

$$f_{100} = \frac{c_0}{2L\sqrt{\varepsilon_r \mu_r}} \tag{2.1}$$

ε_r and μ_r are the relative permittivity and permeability of the substrate, respectively. c_0 is the free space speed of light. The above approximation neglects fringing effects, and the true resonant frequency of the antenna is slightly lower than that predicted by (2.1). However, the principle that the effective electrical length of the patch determines the frequency of operation is an important concept, and this simplistic model provides important intuition for the analyses to follow.

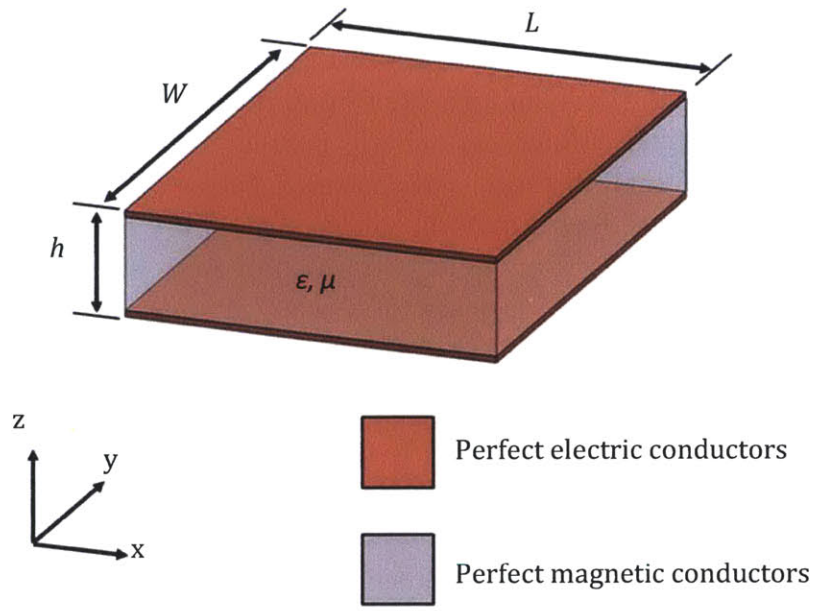

Figure 2.1: Cavity model of rectangular microstrip patch antenna.

Cavity Model

A more accurate model of a patch antenna is what is known as a cavity model. The resonant modes of a patch antenna can be predicted by neglecting radiation altogether and treating the antenna simply as an electrically resonant cavity. By applying perfect electrically conductive boundary conditions along the patch and ground plane surfaces and perfect magnetically conductive boundary conditions around the perimeter of the patch, a dispersion relation function can be found that satisfies the wave equation. The solutions to the dispersion relation are the resonant frequencies of the antenna. An illustration of the cavity model applied to a rectangular patch antenna is shown in Figure 2.1. For the illustrated rectangular patch antenna in Figure 2.1 with height h, length L, width W, permittivity ε, and permeability μ, the general formulation for the resonant frequencies must satisfy the dispersion relation

$$4\varepsilon\mu\pi^2 \cdot f_{mnp}^2 = \left(\frac{m\pi}{L}\right)^2 + \left(\frac{n\pi}{W}\right)^2 + \left(\frac{p\pi}{h}\right)^2 \tag{2.2}$$

$$m, n, p = 0, 1, 2, \ldots; \quad m = n = p \neq 0.$$

It follows from (1.2) that the resonant frequencies are

$$f_{mnp} = \frac{1}{2\pi\sqrt{\varepsilon\mu}}\sqrt{\left(\frac{m\pi}{L}\right)^2 + \left(\frac{n\pi}{W}\right)^2 + \left(\frac{p\pi}{h}\right)^2}. \tag{2.3}$$

m, n, and p are integers corresponding to the order of the antenna modes in the x, y, and z dimensions, respectively. Due to the electrically small substrate height h, variations in the z direction are ignored, leaving p equal to zero and z-directed electric fields. Therefore only transverse magnetic (TM_{mn0}) modes are considered in most patch antenna analyses. Cavity model solutions for the electric field distribution under the patch are shown in Figure 2.2.

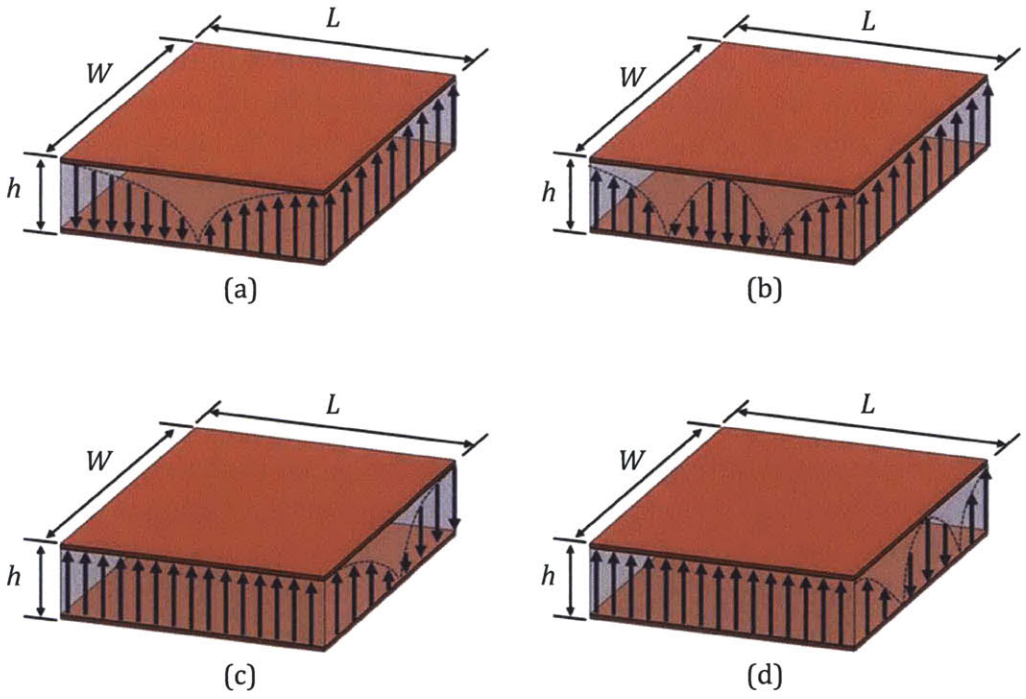

Figure 2.2: Electric field distributions under rectangular patch antenna as predicted by cavity model: (a) TM100, (b) TMM200, (c) TMM010, and (d) TMM020 modes.

As mentioned previously, the typically desired broadside radiation is achieved when the phases of the electric fields under the patch are opposite in sign. Therefore, first order modes, which are cosinusoidal in form, are most commonly used in patch antenna design, although attempts to modify second and third order modes for dual-mode broadside radiation have been made. The resonant frequency f_{100} predicted by the cavity model for the first order length-oriented mode is deduced from (2.3) as

$$f_{100} = \frac{1}{2L\sqrt{\varepsilon\mu}} = \frac{c_0}{2L\sqrt{\varepsilon_r\mu_r}}. \tag{2.4}$$

This solution is the same as that reached by the transmission line model and again emphasizes the role of electrical length in determining the resonant frequency of a patch antenna. However, the cavity model also simultaneously illuminates other potential antenna modes, among which the width-oriented first order mode is most interesting. Again applying (2.3) the first order patch resonant frequency f_{010} in the width-oriented mode is

$$f_{010} = \frac{1}{2W\sqrt{\varepsilon\mu}} = \frac{c_0}{2W\sqrt{\varepsilon_r\mu_r}}. \tag{2.5}$$

The various antenna modes can be excited by proper placement of the antenna feed. The antenna feed position also helps set the input impedance of the antenna and thus the matching necessary for efficient coupling between guided and radiating waves. Although many feeding techniques exist with various advantages and disadvantages, only coaxial probe feeds are used in the antennas explored in this thesis. Coaxial feeds are simple to design and permit great flexibility in impedance matching but are more narrowband than other techniques such as aperture or proximity coupling, which may have advantages for frequency reconfigurable antennas.

Feed effects are not typically included in cavity models in order to reduce complexity. Feed location is best determined through full-wave simulation. Although loss mechanisms can be added to the cavity model to analyze radiation, the pattern is best designed using full-wave simulation. However, the cavity model does reinforce the concept of electrical length and introduces that of antenna modes. These ideas will be necessary to specify not only the operating frequency, but also the polarization of patch antennas.

Polarization Theory

Polarization is an important antenna specification that can determine the suitability of an antenna for a particular application. The polarization of an antenna is usually defined as the time-varying direction and magnitude of the far field plane wave electric field strength transmitted or received at an antenna's main radiation lobe along the direction of propagation. Another common definition references the above definition of polarization to the surface of the Earth. Antennas will not efficiently couple to electromagnetic waves orthogonal to the antennas' own polarization.

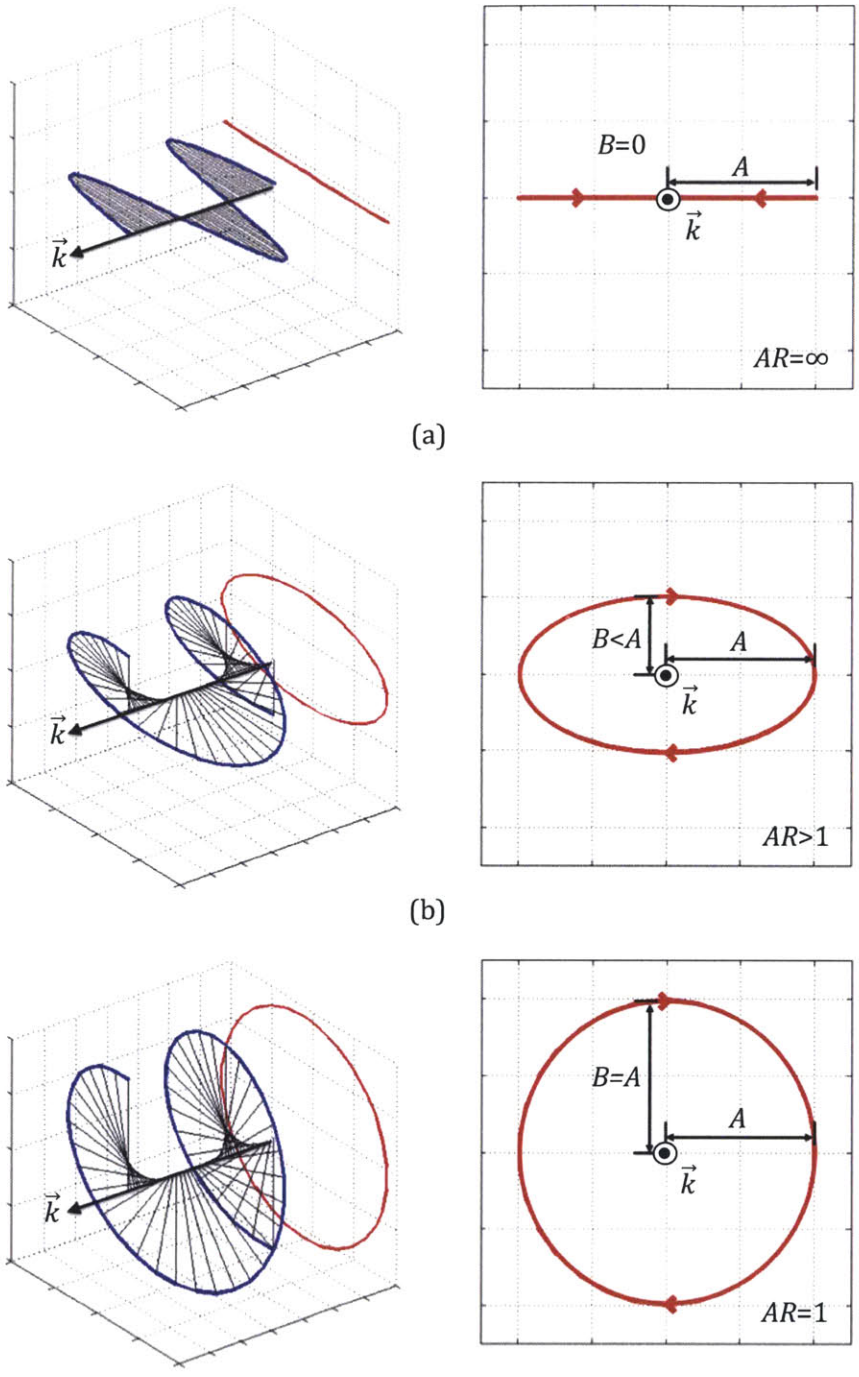

Figure 2.3: Illustrations of (a) linear, (b) elliptical, and (c) circular polarized waves and their respective polarization ellipses.

A simple visualization of polarization is obtained by tracing the path of the electric field vector in time as viewed along the direction of propagation. This image is referred to as a

polarization ellipse. Although polarizations are typically classified as linear, circular, or elliptical, all true waves are elliptically polarized with the linear and circular cases representing limiting cases of ellipticity. Illustrations of various polarizations are shown in Figure 2.3. Axial ratio is the measure of the ellipticity of an antenna's polarization. Mathematically, the axial ratio AR is the ratio of the major axis A to the minor axis B of an antenna's polarization ellipse as described in (2.6) and illustrated in Figure 2.3.

$$AR = \frac{A}{B}; \quad 1 \leq AR \leq \infty \tag{2.6}$$

Perfectly linearly polarized antennas have infinite axial ratios, and perfectly circularly polarized antennas have an axial ratio equal to one. When a circularly polarized antenna is desired, an axial ratio bandwidth is commonly specified. The axial ratio bandwidth is the frequency range over which the axial ratio is within specified limits. Typically the maximum limit for a circularly polarized antenna is set at an axial ratio of 2.

Polarization is not only characterized by axial ratio, but also by a polarization sense that describes the direction of rotation in time of the electric field vector as viewed along the direction of propagation. The polarizations are named such that the time rotation of the electric field vector corresponds to the rotation of the fingers if the thumb is pointed in the direction of propagation. Low axial ratio antennas will not couple efficiently to waves with an opposite polarization sense.

The selection of antenna polarization is application dependent. Often polarizations are adopted simply as conventions for different wireless technologies. Examples are horizontally polarized UHF broadcast television and vertically polarized broadcast radio. Other applications such as GPS and satellite communications specify circular polarizations so that system performance is not significantly dependent on antenna orientation. Mobile handheld technologies such as cell phones also can benefit from the orientation de-sensitivity of circularly or slightly elliptically polarized antennas.

Polarization Control

Microstrip patch antennas can be designed to have either linear or circular polarizations. Taken independently, the modes discussed in the preceding cavity model analysis all result in a linearly polarized antenna. A circularly polarized patch antenna can be achieved by equally exciting two antenna modes that are orthogonal both in physical orientation and in electrical phase at the operating frequency. Equal amplitude and orthogonal space-phase difference of two linear modes are sufficient conditions for circular polarization. For rectangular patch antennas, the two orthogonal modes are typically the TM_{100} and TM_{010} modes of the antenna for reasons previously discussed.

The most intuitive method for achieving two-mode excitation and orthogonal phase relationship is to excite a patch at two adjacent edges and shift one excitation by 90° in phase relative to the other with a 90° hybrid as illustrated in Figure 2.4. Selecting which excitation is phase-delayed controls the sense of polarization. For a rectangular patch, this two-feed method implies that the frequency of operation f_o should be equal to both f_{100} and f_{010}. Therefore, the antenna should be symmetric. This approach for achieving circular polarization is intuitive but structurally complex. Moreover, if a circularly polarized frequency reconfigurable patch antenna is desired, a sufficiently wideband 90° hybrid may not be available.

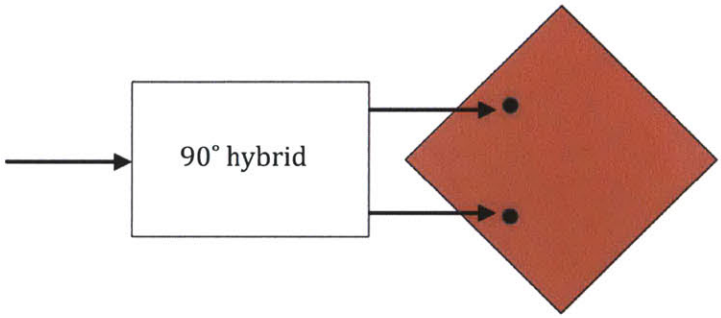

Figure 2.4: Dual-feed method for circular polarization

Although more sensitive than two-feed arrangements, single-feed circularly polarized patch antennas are possible and are better suited to meet the needs of already complex reconfigurable designs. Single-feed arrangements achieve circular polarization by a judicious feed placement that excites two orthogonal modes. These arrangements also introduce asymmetries in the antenna geometry to achieve phase difference through mode degeneracy. Illustrations of common single-feed circularly polarized patch antennas are shown in Figure 2.5.

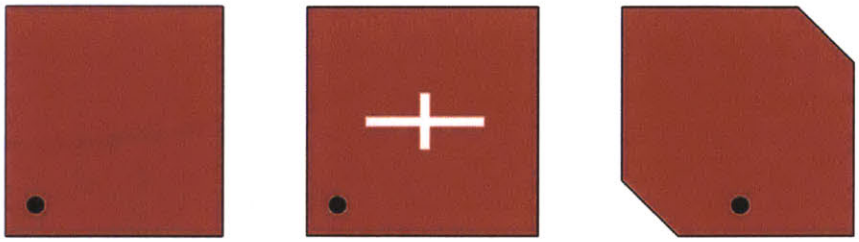

Figure 2.5: Common single-feed patch antenna topologies: (a) near square, (b) asymmetric cross-slots, and (c) corner truncated

For a rectangular patch antenna, the feed should be placed to excite both the TM_{100} and TM_{010} modes, and an asymmetry should be introduced such that f_{100} is precisely different from f_{010} by a small amount. The antenna is then operated at a frequency f_o between f_{100} and f_{010} where the phases of the two modes are 90° apart, thereby meeting the conditions for circular polarization. Plots of single-feed circularly polarized antenna real impedance and impedance phase against frequency are shown in Figure 2.6, illustrating the desired two-mode excitation and phase difference. One major drawback of single-feed circularly polarized patch antennas is their very small axial ratio bandwidths, which are typically fractions of a percent of the operating frequency.

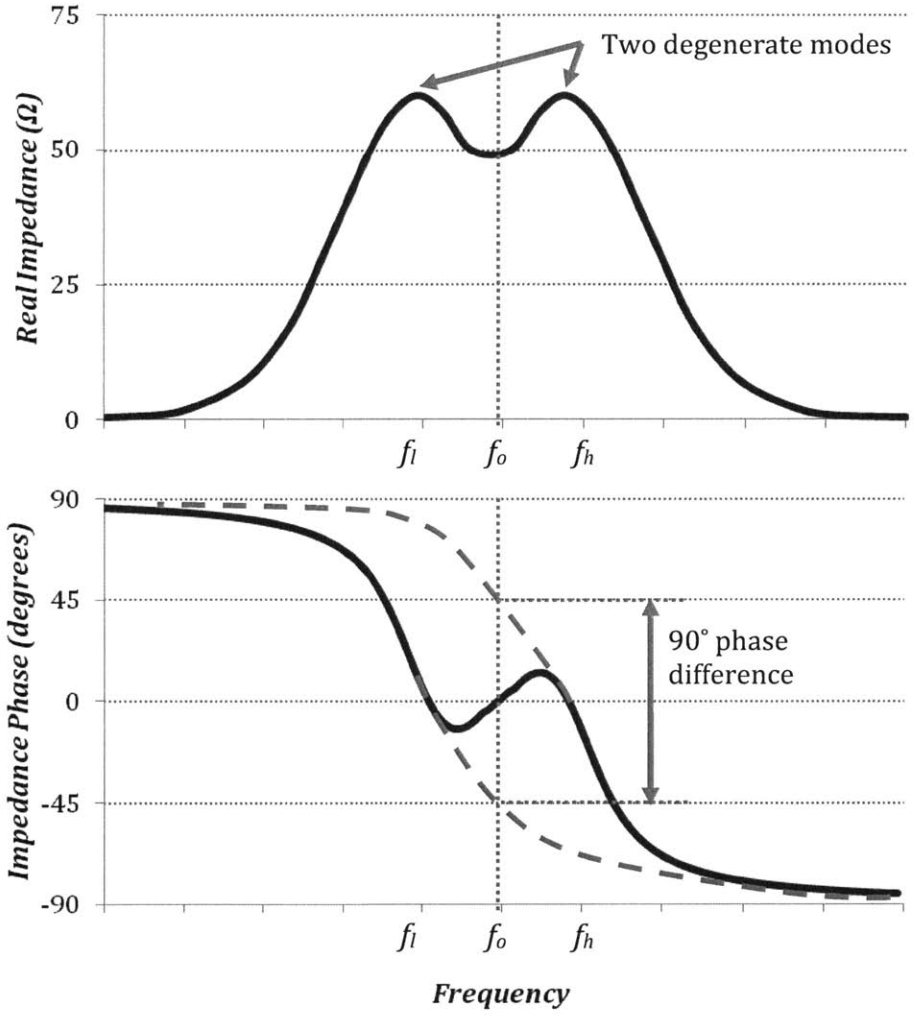

Figure 2.6: Conceptual illustration of single-feed circularly polarized patch real impedance magnitude and phase behavior. Mode phases are shown in dashed lines.

Polarization sense in single-feed patch antennas is controlled by the orientation of the feed with respect to the radiating edges of the two orthogonal antenna modes. Although the feed positions for different polarization senses are often noted in single-feed designs, the physical reasons behind sense determination are not well documented. A simple, concept-based method for sense determination is presented below to provide intuition for sense determination in single-feed circularly polarized patch antennas.

Figure 2.7 illustrates a cross section view of a simplified cavity model solution for the electric field of a first order mode resonance under a patch antenna neglecting the feed. It is clear from Figure 2.7 that the electric field phases at the radiating edges are not only 180° apart, but also that the phase at the edge nearest the feed is most similar to the phase at the feed. This relationship holds throughout an entire period at the frequency of operation for both orthogonal modes. Although the effect of the feed is neglected in the field distribution, this simplified cavity model provides intuition for the important general phase relationships between the feed and the radiating edges and is sufficient for sense determination. Revisiting Figure 2.6, it is seen that the higher frequency mode always leads the lower frequency mode in phase at the operating frequency f_o by 90°. These facts enable the relative phases of the fields under the patch to be mapped, and therefore the polarization sense can be determined as follows.

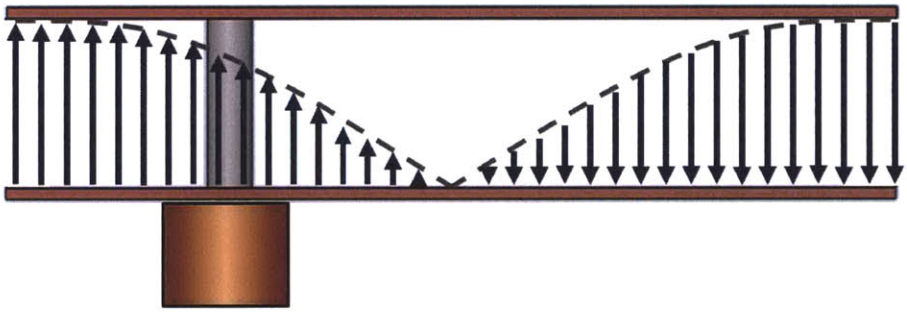

Figure 2.7: Simplified cavity model electric field distribution with feed

The method for sense determinations begins with identifying the nearest radiating edge for the higher frequency and lower frequency modes, respectively. Then, the relative electric field phase is mapped in time, starting with the nearest higher frequency radiating edge, followed by the nearest lower frequency radiating edge, and continuing in the same direction around all the radiating edges of the antenna. The direction of rotation is equivalent to the polarization sense of the antenna noting that for a top view of the antenna, the direction of propagation at the main lobe is out of the page. High and low frequency mode radiating edges are determined using cavity model analysis or by simple arguments of electrical length.

Figure 2.8 illustrates this method applied to the near-square antenna geometry introduced in Figure 2.(a) for both right-hand and left-hand configurations. The high and low frequency radiating edges nearest to the feed are denoted by H' and L', respectively. The high and low frequency radiating edges farther from the feed are denoted by H and L, respectively. A phase reference marker for sense mapping is noted with a red X. This marker corresponds to the nominal phase at the nearest high frequency radiating edge H' at $\omega t = 0$. Note that the only difference between the two configurations is the placement of the feed relative to the antenna asymmetries. In this case, the feed is placed along the diagonals to achieve equal excitation of the two modes.

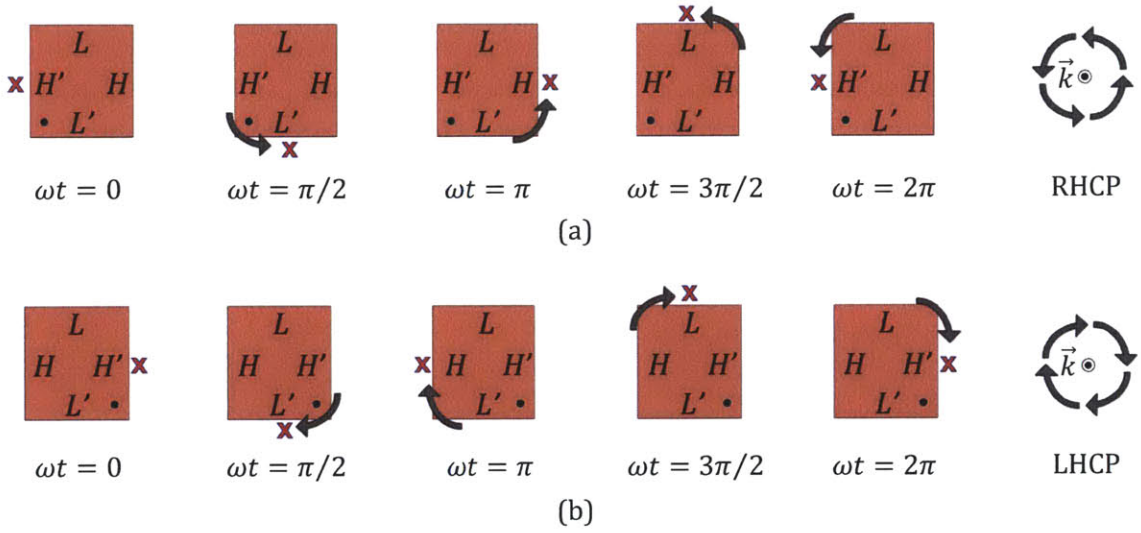

Figure 2.8: Polarization sense determination method applied to (a) RHCP and (b) LHCP near-square patch antenna. Sequence is always H', L', H, L through period.

The antenna geometry in Figure 2.5(c) is a common topology known as a corner truncated square patch antenna. It is widely used in GPS applications. Although the determination of the effective radiating edges is less obvious with the corner truncated square antenna than it is with the near-square antenna, the above method can still be applied. The longer edges still correspond to the primary radiating edges, but the distinction between higher and lower frequency modes must be determined relative to the feed location, which is typically along a centerline of the square. The nearest chamfered corner of the square to the feed can be considered to be a segment of the higher frequency radiating edge, and the analysis can be proceed as before. The antenna as depicted in Figure 2.5(c) is right-hand circularly polarized (RHCP). The corner truncated square patch is the basis for the topology of the circularly polarized frequency reconfigurable antenna explored in this thesis. Frequency and polarization agility will be achieved by switched control of electrical length and the orientation of dominant asymmetries.

Chapter 3

Liquid Metal Microswitches

3.1 Specifications

The broad objectives for a liquid metal microswitch for a reconfigurable microstrip patch antenna include low on-state resistance, bistable operation, and an electronically controllable actuation method. The area of the actuation apparatus should be less than twice the size of the antenna in order to provide a footprint advantage over a multiple antenna implementation. It should also leave as much area as possible for the radiating patch in order to maximize antenna gain.

Other specifications imposed on the switch include a thickness limit of 25mils – substrate excluded, mercury content less than 0.5mg, and a switch footprint on the order of 0.1mm^2. The thickness and footprint constraints are limits determined by the size specifications for the reconfigurable patch antenna, which must accommodate as many as 30 switches within a 10.24cm^2 area and be no more than 110mils thick in total. The mercury level constraint minimizes toxicity concerns by limiting the quantity of mercury to approximately the same amount contained in three average compact fluorescent light bulbs [19].

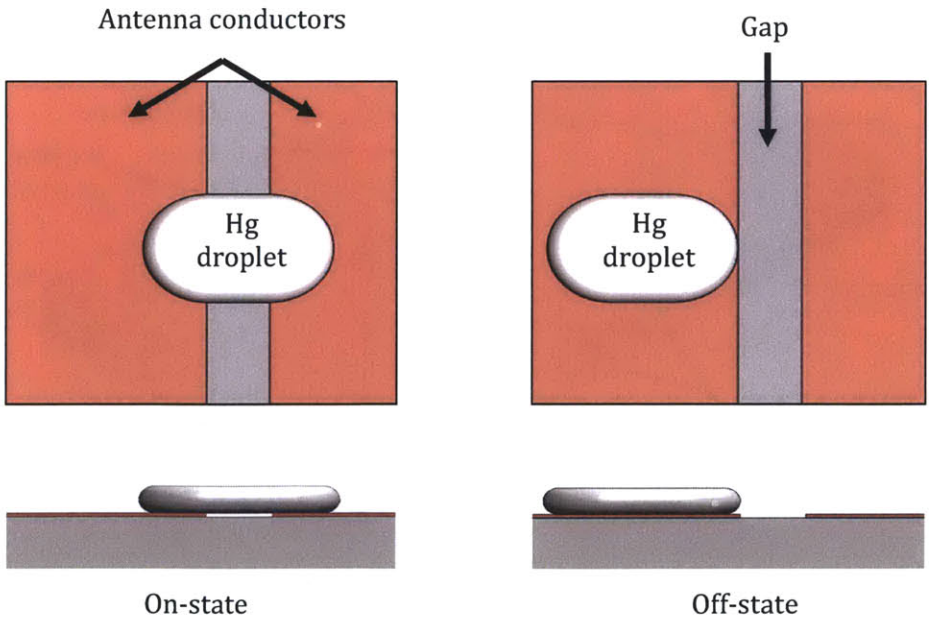

Figure 3.1: General topology for liquid metal microswitch for reconfigurable patch antenna

To meet these objectives, a general topology independent of any actuation method is proposed as illustrated in Figure 3.1. In the on-state, a mercury droplet electrically connects two solid conductors that represent different elements of the antenna. In the off-state these antenna elements are electrically isolated by a gap, and the mercury droplet is positioned on top of one of the antenna elements. This topology maximizes the area available to the antenna elements because no conductors besides the mercury droplet share the same plane as the antenna elements. Structures should be included to ensure bistable operation and thus low power consumption of the switch when holding a configuration. The switch should include a cover and some form of lateral containment for the mercury droplet for both actuation and safety reasons.

Of course, the details of actuation cannot be ignored, and the choice of actuation method will determine the performance and specific geometry of the microswitches. The following sections explore the design of both fluidically and electrostatically actuated liquid metal microswitches and conclude with a comparison of the two designs.

3.2 A Fluidic Switch

Principle of Operation

A conceptual illustration of the proposed fluidically actuated liquid metal microswitch is shown in Figure 3.2.

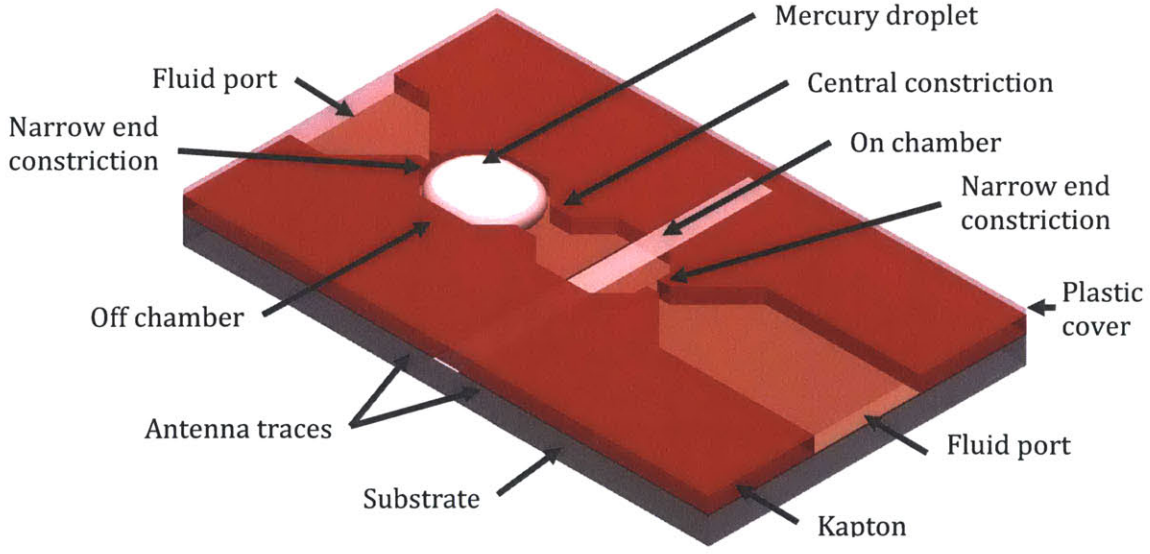

Figure 3.2: Fluidically actuated liquid metal microswitch

A liquid metal droplet is confined in an enclosed channel with a non-uniform cross section on top of the surface of an antenna. The channel is comprised of two chambers separated from each other and from the fluidic ports by three constrictions. The droplet is actuated between the two chambers by externally applied pressures acting through a dielectric working fluid. The chambers correspond to on and off-states of the switch. The on-state chamber overlays two solid metal antenna elements separated by a gap. The off-state chamber overlays a single metal antenna element. The role of the central constriction is to provide a surface tension pressure threshold for robust actuation control. The narrower constrictions to the fluidic ports provide high surface tension barriers that prevent the droplet from escaping the switch structure. Without these pressure barriers, the mercury droplet would escape the structure, and only a completely liquid metal-filled channel could be reliably actuated, greatly increasing the mercury content of the device.

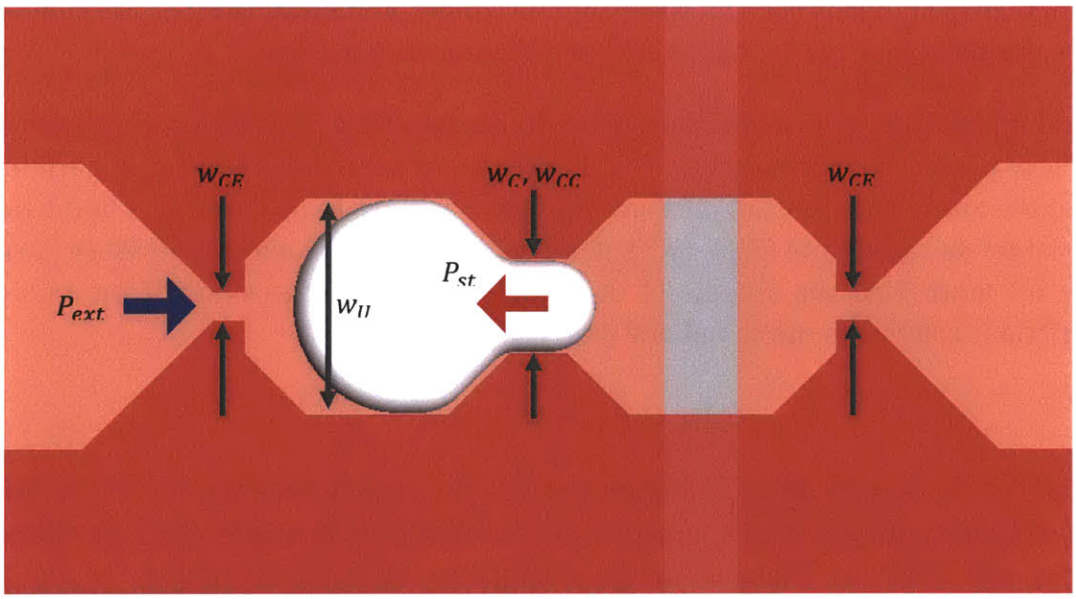

Figure 3.3: Fluidic switch operation

The operation of the switching mechanism can be explained in terms of pressure barriers created by the constrictions in the microfluidic structure. These pressure barriers arise from the surface tension of the liquid metal droplet as its radii conform to a microfluidic constriction. The intrinsic surface tension at a fluid boundary results in a force that acts to minimize the surface energy of a fluid. For a droplet in an enclosed channel, this force is seen as a pressure difference ΔP_x across a fluid boundary and can be related to the surface tension γ of the fluid and the droplet's principal radii of curvature R_v and R_h, corresponding to the vertical and horizontal radii, respectively, using the Laplace equation given by

$$\Delta P = \gamma\left(\frac{1}{R_v} + \frac{1}{R_h}\right). \tag{3.1}$$

The surface tension of mercury can be approximated as 0.4 N/m [26]. An enclosed droplet's principal radii of curvature R_v and R_h can be expressed as functions of the contact angle θ_c of the fluid system and the height h and width w of the structure as given in (3.2).

$$R_v = \frac{h}{2\,cos(\theta_c)} \qquad R_v = \frac{w}{2\,cos(\theta_c)} \tag{3.2}$$

The contact angle is itself a function of the surface tensions at the fluid-fluid and fluid-solid boundaries and is dependent on the properties of the specific fluids and solid surfaces involved. For mercury droplets on the materials commonly used in microfluidic devices and microstrip antennas such as SU-8, Kapton, copper, and RF substrates, the contact angle can be approximated as 140° based on experimental observations.

A liquid metal droplet in a confined structure has two fluid boundaries, each with its own interfacial pressure difference ΔP_x. The difference between the pressures at each interface defines the net surface tension pressure P_{st}, which is given in (3.3) and acts in the direction of the larger surface. From (3.1)–(3.3), it is clear that a surface tension pressure barrier can be set by controlling the volume of the droplet and the dimensions of the microfluidic constrictions relative to the chambers' dimensions.

$$P_{st} = \Delta P_1 - \Delta P_2 \tag{3.3}$$

If an external pressure ΔP_{ext} is imposed across the switch structure such that the liquid metal droplet is forced into a constriction as illustrated in Figure 3.3, the droplet will displace and begin to conform to the dimensions of the constriction. As the droplet displaces into the constriction, the fluid interface at the constriction narrows, resulting in an increasing surface tension pressure P_{st} that opposes the imposed external pressure up to a maximum pressure P_b given by

$$P_b = P_{st,max} = \gamma\left[\left(\frac{1}{R_{vU}} + \frac{1}{R_{hU}}\right) - \left(\frac{1}{R_{vC}} + \frac{1}{R_{hC}}\right)\right], \tag{3.4}$$

where R_{vU}, R_{hU}, R_{vC}, and R_{hC} are the vertical radius of the unconstricted left interface, the horizontal radius of the unconstricted left interface, the vertical radius of the constricted interface, and the horizontal radius of the constricted interface, respectively. For a microfluidic structure of uniform height, (3.4) can be simplified to (3.5) where w_U and w_C are the widths of the unconstricted left interface and the constricted interface, respectively.

$$P_b = 2\gamma cos\,(\theta_c)\left(\frac{1}{w_U} - \frac{1}{w_C}\right) \tag{3.5}$$

If the maximum surface tension pressure barrier P_b of a constriction is greater than the imposed external pressure P_{ext}, the droplet displaces along the external pressure gradient until equilibrium is reached and the surface tension pressure balances the external pressure. If the maximum surface tension pressure barrier P_b of a constriction is less than the imposed external pressure P_{ext}, the droplet will pass through the constriction and continue. The theoretical barrier pressure for a mercury droplet in silicone oil with a 140° contact angle in a channel of uniform height is plotted against the ratio of the constricted and unconstricted widths seen by the droplet's interfaces in Figure 3.4.

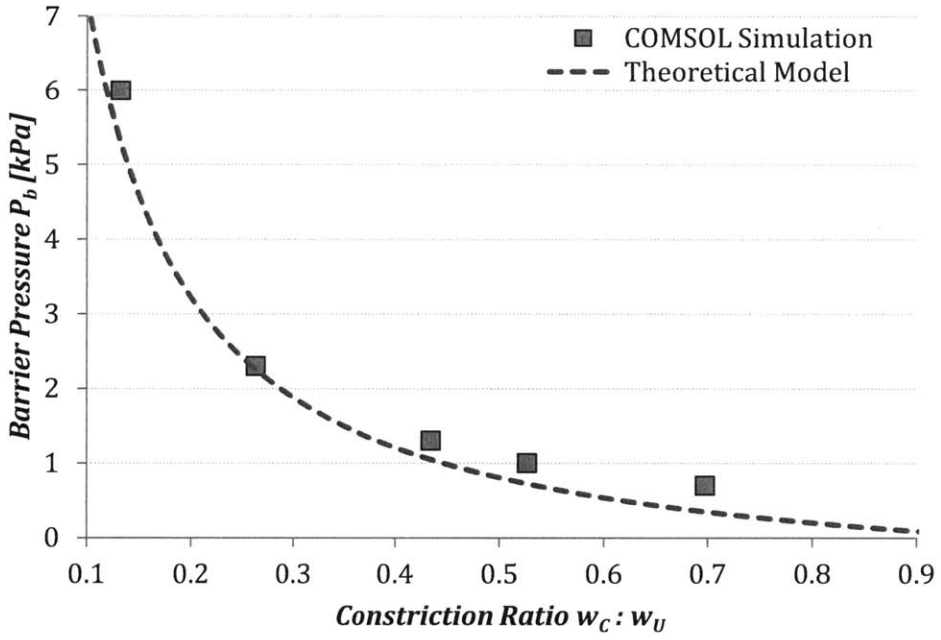

Figure 3.4: Theoretical and simulated surface tension pressure barrier versus constriction ratio

Although the preceding analysis is completed only in one direction for the central constriction, the same analysis can also be applied to the narrower constrictions at the far ends of the switch chambers and in both directions. By dimensioning the central constriction to be wider than the constrictions at the ends of the switch, a range of operating switch actuation pressures can be established between $P_{b,center}$ and $P_{b,end}$, corresponding to the maximum surface tension pressure barriers provided by the center and end constrictions, respectively. The central constriction with width w_{CC} sets the minimum actuation pressure to displace the liquid metal droplet from one chamber to the other. The end constrictions with width w_{CE} set the maximum allowable actuation pressure such that the droplet does not escape the switch structure.

The importance of interface pressures and surface tension in this model suggests that the working fluid should have low viscosity to reduce resistance in the channels leading to the switch and low surface tension to complement the high surface tension of mercury. Low surface tension fluids also wet surfaces well, reducing the chance of air bubbles interrupting switch operation. A variety of silicone oils are available that are low conductivity, low viscosity, and low surface tension. Dow Corning 317667 5cSt silicone oil was selected as a working fluid for the switch.

In practice, the required actuation pressure is higher than that predicted in (3.5) due to contact angle hysteresis and fluidic resistance in the whole path from pressure source to switch. Therefore, the true actuation pressure should be determined experimentally. However, as demonstrated in the following sections, the relationship between width ratio and relative pressure barrier level holds and allows for fluidic control of the switch.

Finite-Element Model Simulation

To verify the relationship predicted in (3.5), a 2-D finite-element time domain simulation of the fluidic switch was conducted using the laminar two-phase flow module in COMSOL as illustrated in Figure 3.5.

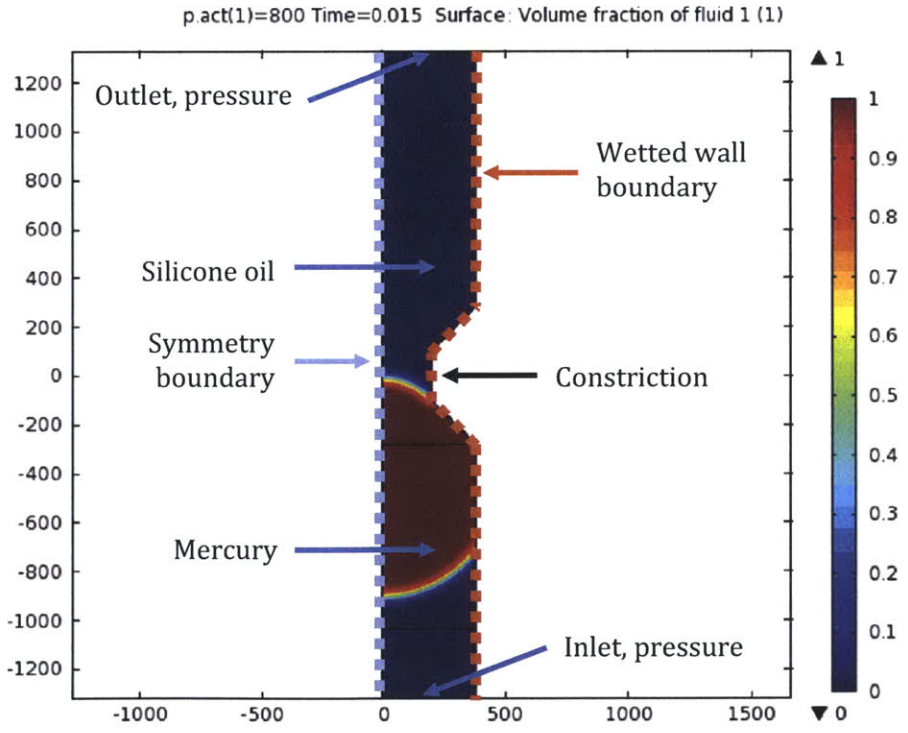

Figure 3.5: COMSOL model of single fluidic constriction

The phase field method was applied with the mobility tuning parameter set to 0.05m-s/kg. The chamber width was fixed at 750μm and the width of a single constriction was varied between 100–530μm, corresponding to width ratios between 13–70%. The length of the constriction is 200μm. A constant channel height of 200μm or about 8mils was assumed. A wetted wall boundary condition is enforced along the sides of the channel with a contact angle of 140°. A 0.5mg mercury droplet is initially positioned within the channel, and all other domains are considered to be 5cSt silicone oil. A constant pressure inlet is assigned to one end of the channel, and a zero pressure outlet is assigned to the opposite end. Incompressible fluid and shallow channel approximations are used. Surface tension coefficient is designated at 0.4N/m. The resistance provided by the channel and the constriction is not taken into account in the theoretical model presented in the previous section, but it is accounted for in the COMSOL model. Symmetry is used to reduce the numerical size of the model.

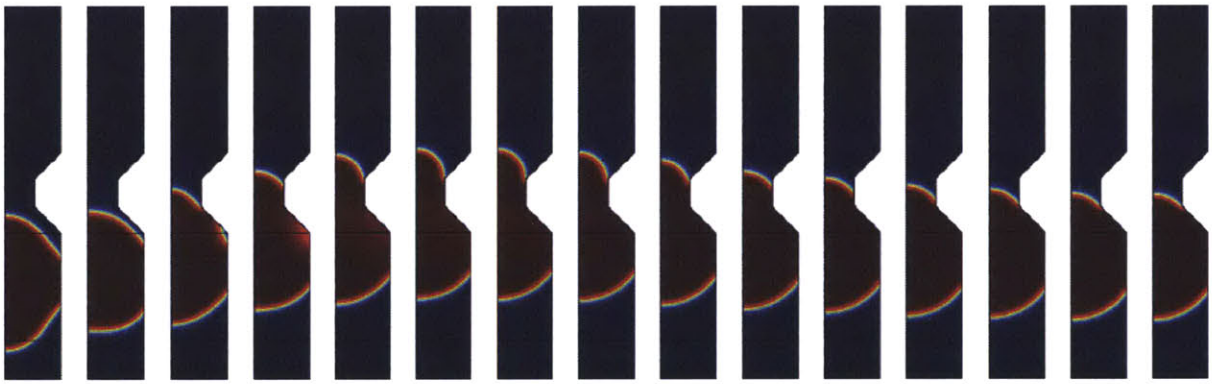

(a)

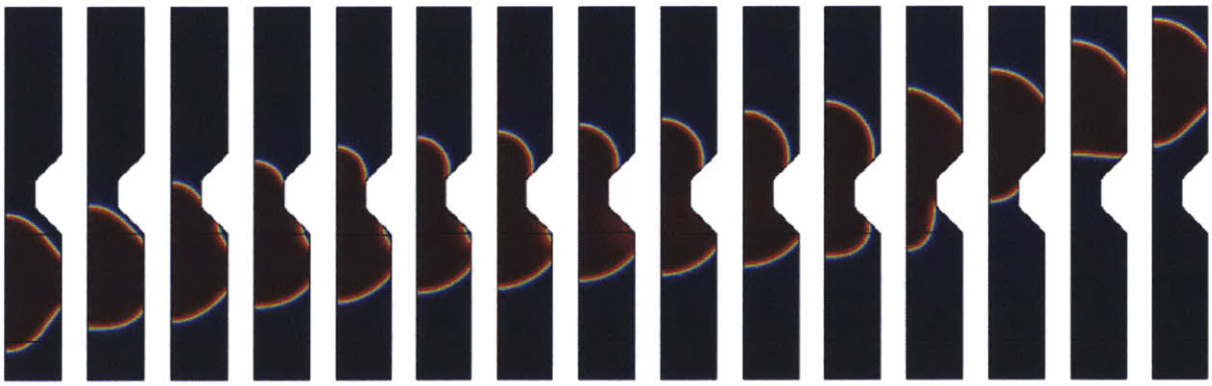

(b)

Figure 3.6: COMSOL time domain simulation results channel with constriction ratio of 53% and an applied pressure of a) 800Pa and b) 1000Pa. Time increases from left to right in 1ms increments. Actuation is observed for 1000Pa but not for 800Pa input pressure.

Iterative simulations were performed with parameterized actuation pressure at the inlet boundary to determine the pressure barrier presented by the constriction. If the mercury droplet came to a full stop at the constriction and did not pass through the constriction within 30ms, the pressure applied at the inlet was determined to be below the surface tension barrier presented by the constriction. If the mercury droplet moved through the constriction at a simulated inlet pressure as illustrated in Figure 3.6(b), a finer parameter sweep of actuation pressure was then performed to obtain a more precise solution for the pressure barrier value. The simulation results are summarized in Figure 3.4 and compared to the threshold pressures predicted in (3.5). Due to the large number of simulations required to determine a very precise solution for the pressure barrier, the simulation results may overstate the pressure barrier by less than 0.2kPa.

The simulated results indicate actuation barriers greater than those theoretically predicted for wider constrictions. This discrepancy reflects the fact that the theoretical model neglects the angled portions of the modeled channel and the channel resistance up to the barrier. This resistance, which can be approximated as the resistance of a channel with a rectangular cross section, becomes significant with respect to the surface tension pressure barrier when constrictions are wide. However, the simulation results indicate that the theoretical model is reasonable and that properly dimensioned constrictions can result in a safe operating range of actuation pressures for the proposed fluidic switch.

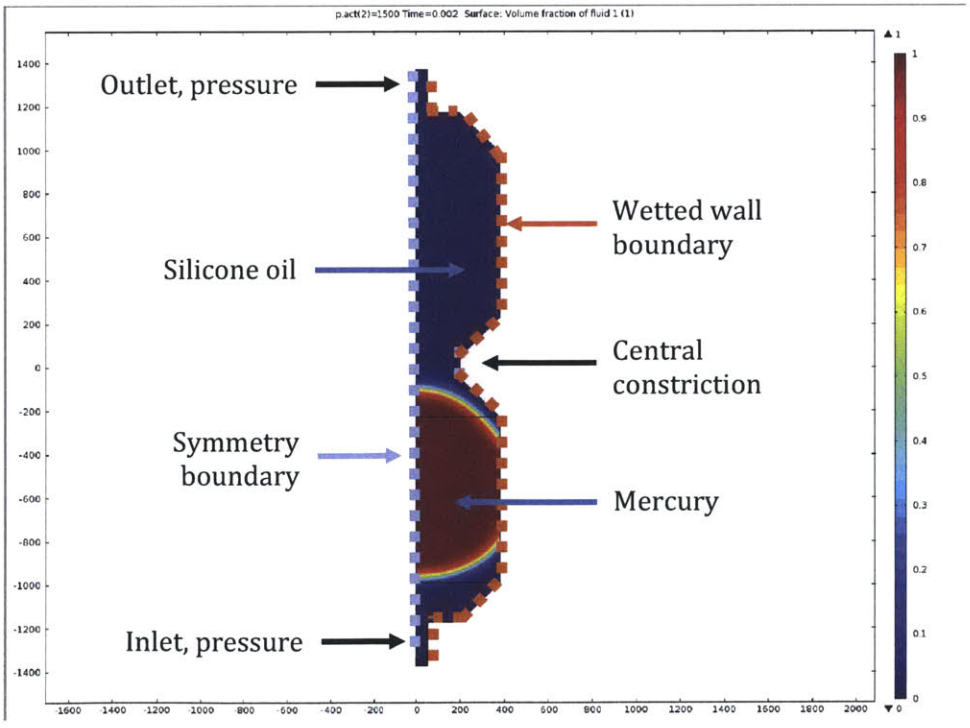

Figure 3.7: COMSOL simulation model for fluidic microswitch

To verify that the theoretical model can indeed be used to design a controllable fluidic switch, the simulation method described above was applied to the complete switch geometry as shown in Figure 3.7.

The chamber width is again set to 760μm. The constrictions at the inlet and outlet are dimensioned to be 100μm or 13% of the chamber width. The central constriction is varied between 200–530μm or 25–70% of the channel width. Again, iterative sweeps of actuation pressures were conducted, and the simulated position of the mercury over time was monitored. Representative simulation results are shown in Figure 3.8. Summarized simulation results are compared to the theoretical model predicted by (3.5) in Figure 3.9.

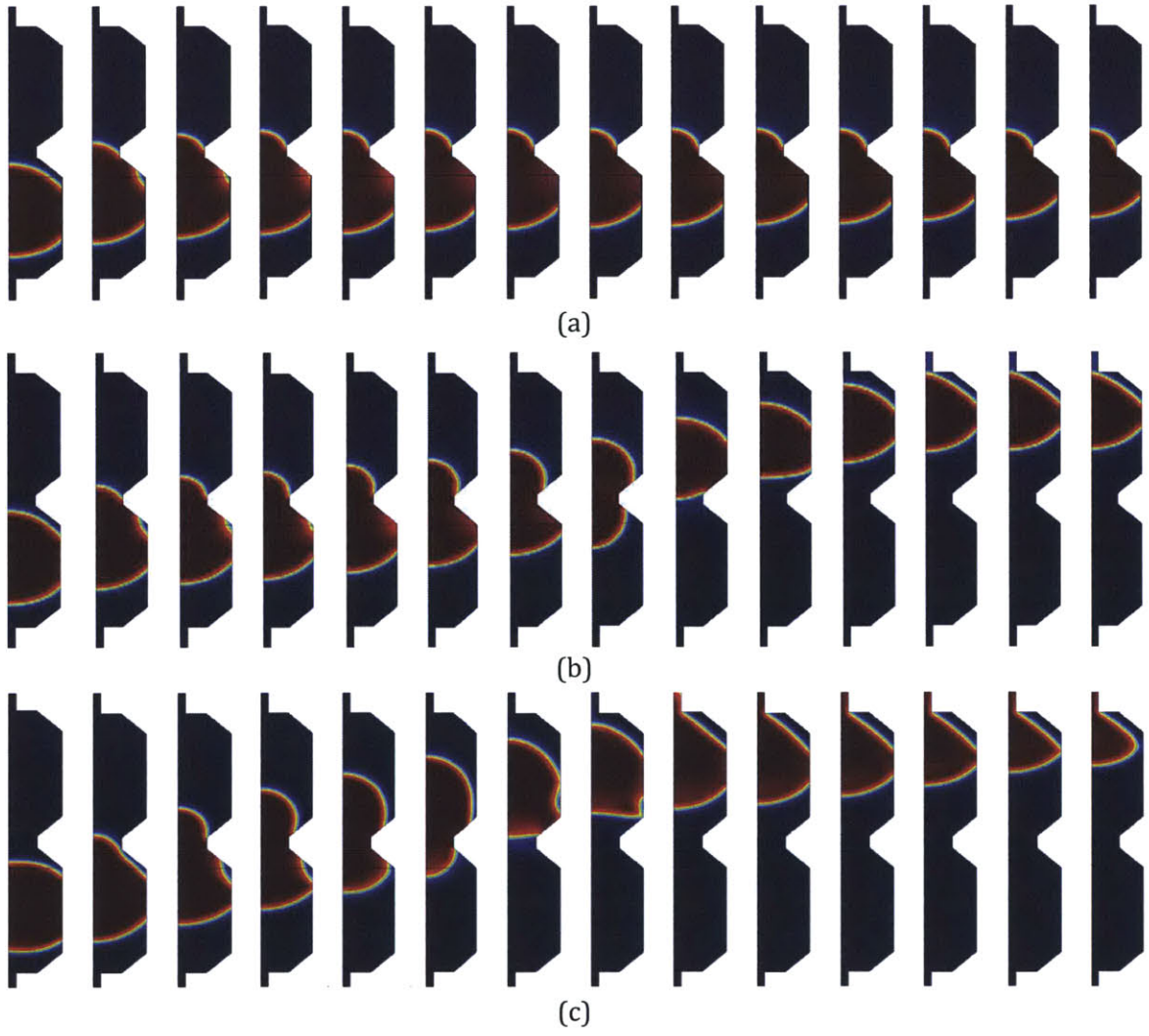

Figure 3.8: Time domain simulation results for switch with 13% end constriction ratio and 53% central constriction ratio for applied pressures of (a) 1.3kPa, (b) 1.5kPa, and (c) 5.5kPa. No actuation is observed in (a). Safe actuation is observed in (b). Droplet escape is observed in (c).

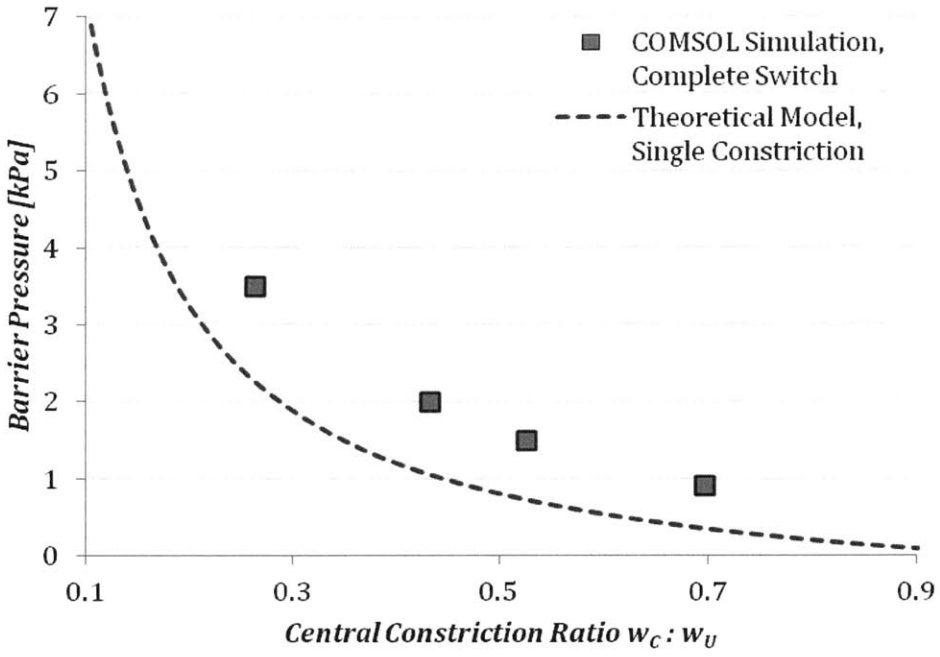

(a)

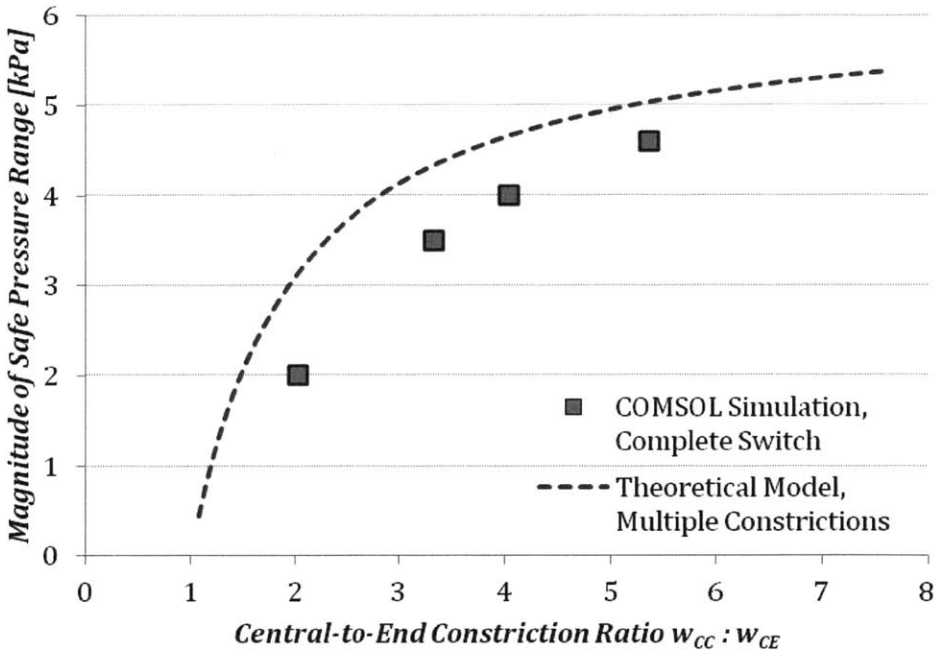

(b)

Figure 3.9: Theoretical and simulated (a) barrier threshold pressures and (b) range of safe operating pressures for complete switch structure.

The trends predicted by the theoretical model of the fluidic switch are observed in the simulated results. However, some differences have important implications for design. The

difference between predicted and simulated absolute pressure threshold shown in Figure 3.9(a) is expected because, again, the theoretical model neglects the total channel resistance. In the case of the complete switch, the channel resistance is significant for the entire range of simulated central constrictions due to the narrow 100μm constrictions at the ends of the switch. These narrow constrictions reduce the pressure available for actuation at the mercury-silicone oil interface.

A more important result of the simulations is that the magnitude of the simulated safe operating pressure range is significantly lower than that predicted by the difference in central-to-end constriction ratios derived by the theoretical model as shown in Figure 3.9(b). The difference ranges from about 0.5kPa at larger central-to-end constriction ratios to 1kPa at central-to-end constriction ratios close to unity. Therefore, the theoretical model should be used conservatively when the central constriction is about equal in size to the narrow constriction.

Fabrication

A prototype switch structure was developed based on the preceding modeling and simulation results. A number of processes were explored in the development of the prototypes. An illustration of the final prototype layout is shown in Figure 3.10. Dimensions are outlined in Table 3.1.

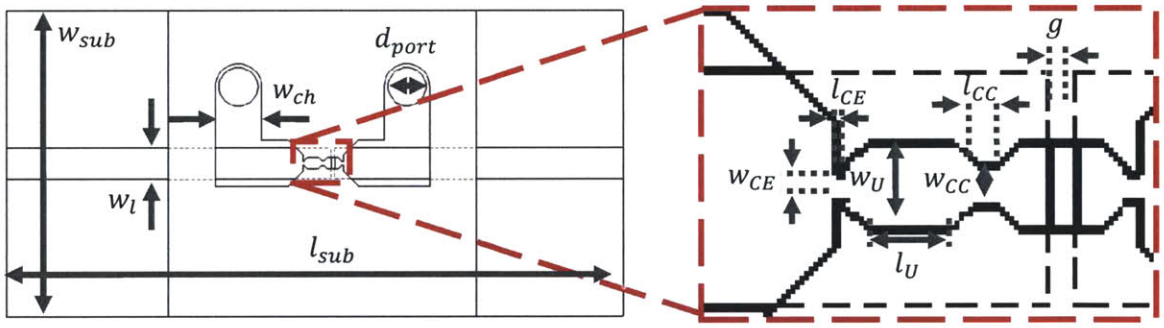

Figure 3.10: Layout of prototype fluidic switch

Table 3.1: Dimensions of prototype fluidic switch

w_{sub}	l_{sub}	w_l	w_{ch}	d_{port}	w_{CE}	l_{CE}	w_U	l_U	w_{CC}	l_{CC}	g
20 mm	40 mm	2.6 mm	3 mm	2.5 mm	100 μm	100 μm	760 μm	750 μm	380 μm	200 μm	250 μm

The microfluidic channels were defined in a Kapton film, and a transparent plastic cover was laminated on top of the switch structures. The circuit was implemented on a copper-plated FR4 circuit board substrate. The channel height was set to 125μm vice the simulated

200μm because 125μm is a readily available film thickness. The reduced height, while expected to increase the absolute required actuation pressure, was not expected to jeopardize switch operation because the 25kPa pressure rating of the selected pump exceeded the expected threshold pressure levels estimated to be on the order of 1kPa.

The switch fabrication process was conducted as follows:

1. Solid metal traces comprising the circuitry of the switch were first milled in the circuit board substrate. Copper on FR4 was used for actuation tests only. Copper on TMM10i was used for RF measurement.
2. 3M467 double-sided adhesive transfer tape was applied to both sides of the 5mil Kapton fluidic layer material under 50psi pressure for 1min.
3. The Kapton and attached adhesives were milled together on a PCB milling machine to form the channel outlines.
4. The Kapton layer was then attached to the circuit board with the adhesive transfer tape under 50psi pressure for 1min.
5. A 0.5mg mercury droplet metered by a controlled growth mercury electrode dispenser was placed into the off-chamber of the switch, and the channels were pre-wetted with silicone oil using a syringe.
6. The 10mil plastic covers were then attached to the top of the fluidic layer under 20psi pressure for 1min using the adhesive transfer tape.
7. Lastly, microfluidic tubes were inserted, glued, and sealed in place at the inlet and outlet ports with a room temperature epoxy.

A photograph of a completed switch prototype is shown in Figure 3.11.

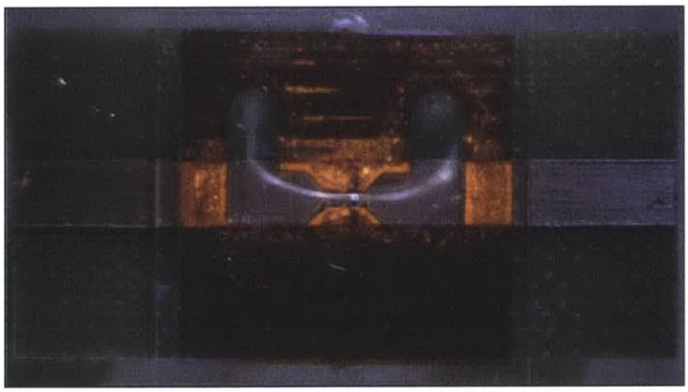

Figure 3.11: Photograph of fabricated fluidic switch prototype

The fabrication process described above was developed based on limited available resources and safety concerns associated with the use of mercury. Circuit board techniques such as milling were favored over cleanroom processes like photolithography due to limited cleanroom access and desire for low cost design iteration. Although laser milling of Kapton is preferable to mechanical milling, most of the prototypes were milled mechanically, again, due to resource availability. Mechanical milling leaves a rougher outline than laser milling or photolithography, and the edges had to be de-burred by hand.

An adhesive transfer tape method was used in place of traditional bonding or even lamination because exposing mercury to high temperature processes would pose a safety hazard. The boiling point of mercury falls from 357°C at atmospheric pressure to 120°C at 100Pa, a temperature below those of many lamination processes using vacuum. Although the vaporization and selective condensation of mercury on gold pads was actually leveraged in [27] to achieve a controllable process for mercury droplet deposition, the facilities for such a process were not available. Tape was applied to both sides of the fluidic layer instead of on the bottom sides of both the fluidic and cover layers because droplets were found to adhere to exposed tape if it covered a channel.

Test devices for the proposed switch featuring only a single constriction were successfully made using lamination and spin-on UV-cured adhesives, but they relied on the ability to flow mercury droplets towards the constriction *after* the device had been closed. This filling method would be difficult to control with a complete switch structure including the narrow end constrictions because the pressure barrier presented by those constrictions would have to be breached at the inlet but not at the outlet. To achieve that, the inlet constriction would likely need to be widened, resulting in reduced safe operating pressure range. Furthermore, in an antenna design with multiple switches, designing a manifold network for filling and actuating multiple switches at a time would be very difficult. Depositing mercury droplets before sealing the device reduces manifold complexity but limits the process to low temperature methods thenceforth.

An earlier version of the process employed lamination until mercury filling, but the difficulties of milling just the tape forced the tape to be present during the lamination process. During lamination, the tape would flow into the channels, and although removal of the excess adhesive was possible, the task was painstakingly labor intensive. Therefore a completely low temperature process was selected to minimize safety hazards while avoiding device failure or large amounts of manual labor. The proposed process is by no means ideal; it is an attempt at a compromise based on resources available to the project.

Mercury amalgamates with copper, and the copper switches described here were expected to be unstable in the long term. Other metals such as platinum were investigated in the realization of the electrostatic microswitches discussed in following sections.

Measurements

Persistent difficulties plagued the fabricated prototypes. Sealing in particular was an issue, with seals proving leaky for almost 50% of the fabricated devices. The loss of pressure in these devices clearly precluded any actuation. Those prototypes that did seal proved more difficult to actuate than anticipated. The Bartels mp5 micropump used in testing could not provide sufficient pressure to move the droplet even in a wide channel, pointing to higher than anticipated friction forces. Droplet movement was sometimes observed when disconnecting the pump from the switch due to the release of vacuum. However, this pressure exceeded the safety limit set by the end constrictions, and the droplet escaped the switch structure. Due to these difficulties, dynamic measurements were not taken.

Static ohmic resistance of the switches in the on-state was measured using a 4-point technique with an Agilent 34401A digital multimeter. The average on-state resistance was 43mΩ. Isolation better than 10dB and insertion loss less than 0.6dB up to 4.5GHz were measured with an Agilent E8363B network analyzer as shown in Figure 3.12. Although the switch structure is not directly representative of the actual insertion loss or isolation seen in any specific patch antenna geometry, the general operation of the device at the frequencies of interest is verified by the measurements. It is also noted that the test structure is not optimized for isolation or return loss but is simply meant to demonstrate sufficient selective connectivity between antenna traces.

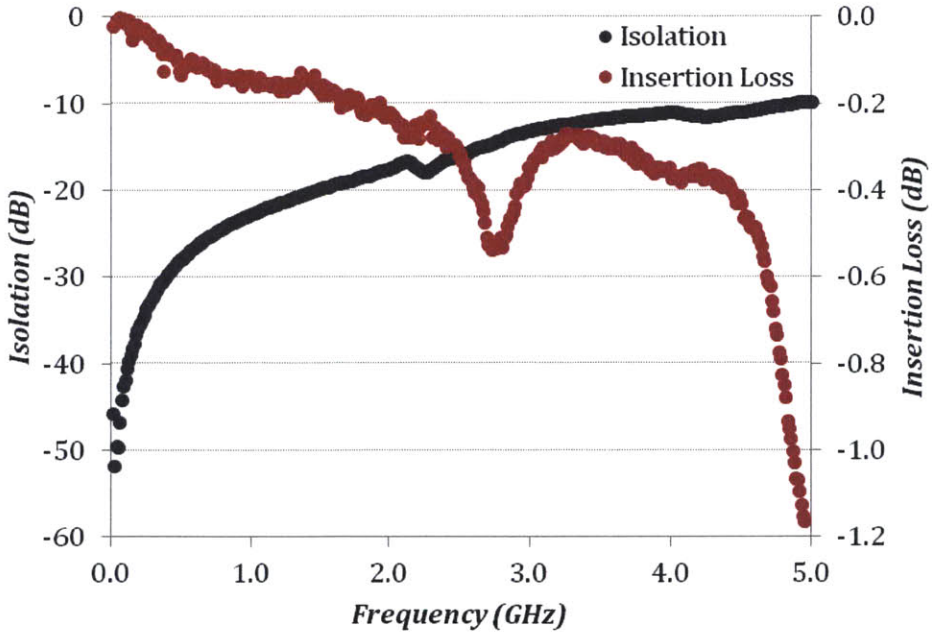

Figure 3.12: Measured fluidic switch isolation and return loss

Two other critical issues with fluidic actuation besides the obvious difficulty in actuation became apparent during the fabrication and measurement process. First was the lack of a suitable, compact bi-directional pump that could not only actuate the switch, but also do so in both directions. Implementing a complete system with a unidirectional pump such as the one used in testing would require an intricate, controllable microvalve system. Secondly, the fluidic actuation system proved cumbersome and messy due to spillage of silicone oil or device leakage. Although testing in a laboratory environment is greatly simplified by the use of glassware and external reservoirs, integration with further electronics would require a rugged design. The challenges of fluidic actuation are not insurmountable, but their difficulty suggests that alternative mechanisms may be more suitable for antenna applications. One such alternative is explored in the following section.

3.3 An Electrostatic Switch

Principle of Operation

Due to the practical difficulties of integrating fluidically actuated microswitches with a patch antenna, an alternative actuation method was developed based on electrowetting-on-dielectric (EWOD) techniques. A conceptual illustration of the proposed switch is shown in Figure 3.13. Inspired by the work in [28], this method uses voltages applied by electrodes across a thin dielectric film to manipulate the mercury droplet in the switch. The electrodes can be solid conductors energized in sequence to achieve droplet translation, or the electrodes can be energized conductive electrolyte droplets that are moved by some other means and pull the mercury droplet along with them. Both electrode types will be demonstrated, although the latter is mostly useful only as a prototyping measure.

The mercury droplet is grounded through the primary antenna radiator. Since the droplet always contacts the primary antenna structure regardless of switch position, this grounding is convenient and can take the place of the grounding plate in traditional EWOD schemes. Although the antenna traces are thus grounded with respect to a low frequency actuation voltage, a bias tee can be used such that the antennas can still act as energized radiators at higher frequencies. The bias tee can also be applied to one end of a switch.

Despite the nomenclature, EWOD is conceptually no different than electrostatic actuation applied to a fluid system [29]. The main advantage of EWOD techniques over fluidic actuation schemes is in direct, localized electrical control of droplet position. The electrode arrays of EWOD systems are precise compared to enclosed channel microfluidics that rely on external pressures. The control advantages of EWOD complement the requirements of the proposed liquid metal switch, which are fundamentally concerned with droplet control. The primary disadvantage of EWOD from an antenna standpoint is the parasitic presence of electrodes. However, it will be shown that by using the antenna as a grounding electrode

and keeping the size of the control electrodes small, this parasitic effect can be minimized. Another disadvantage of EWOD is that actuation can require voltages on the order of hundreds of volts, although voltages as low as 20V have been used successfully [30].

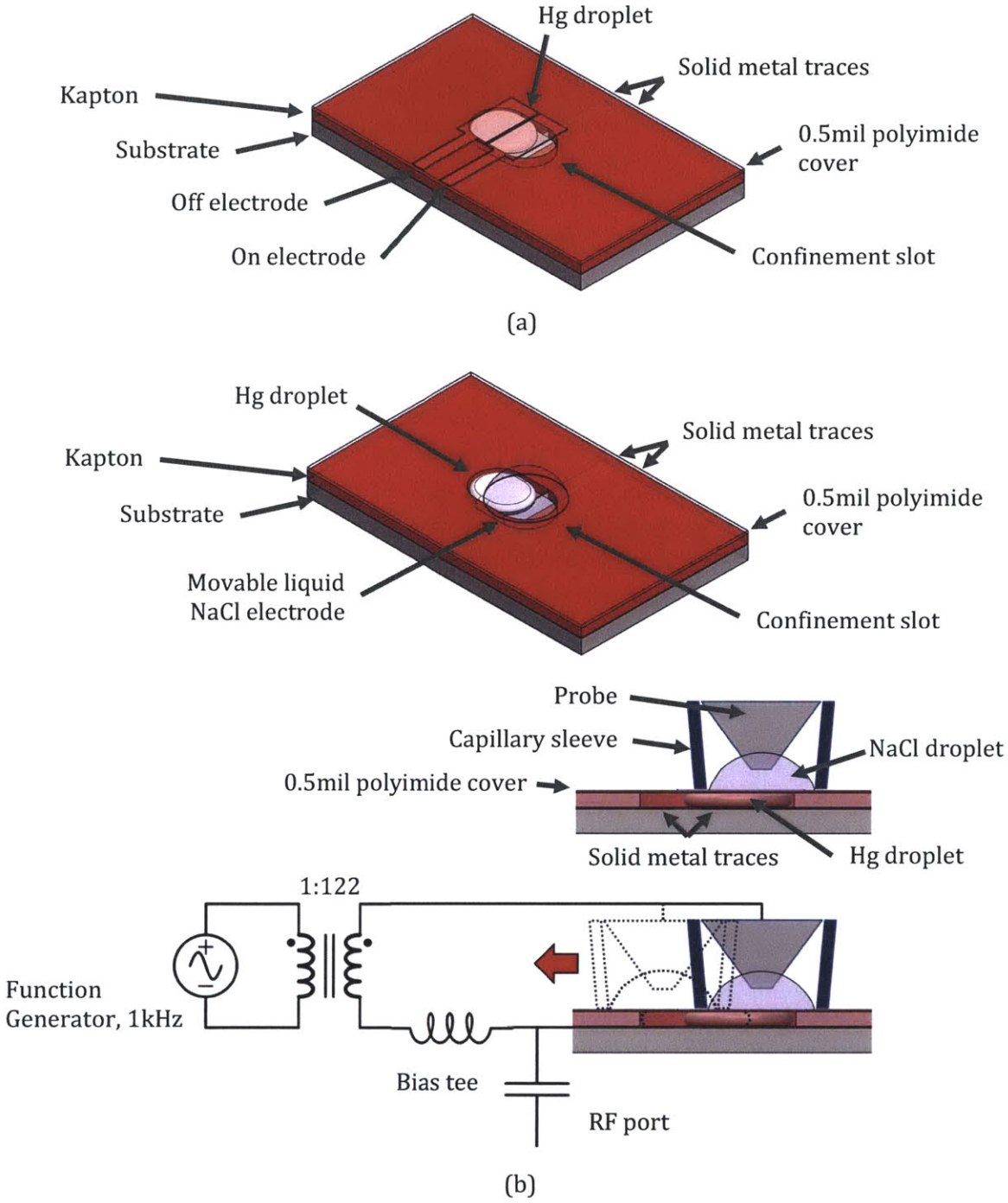

Figure 3.13: Electrostatically actuated liquid metal microswitch with (a) solid electrodes and (b) movable solid electrode using a stylus

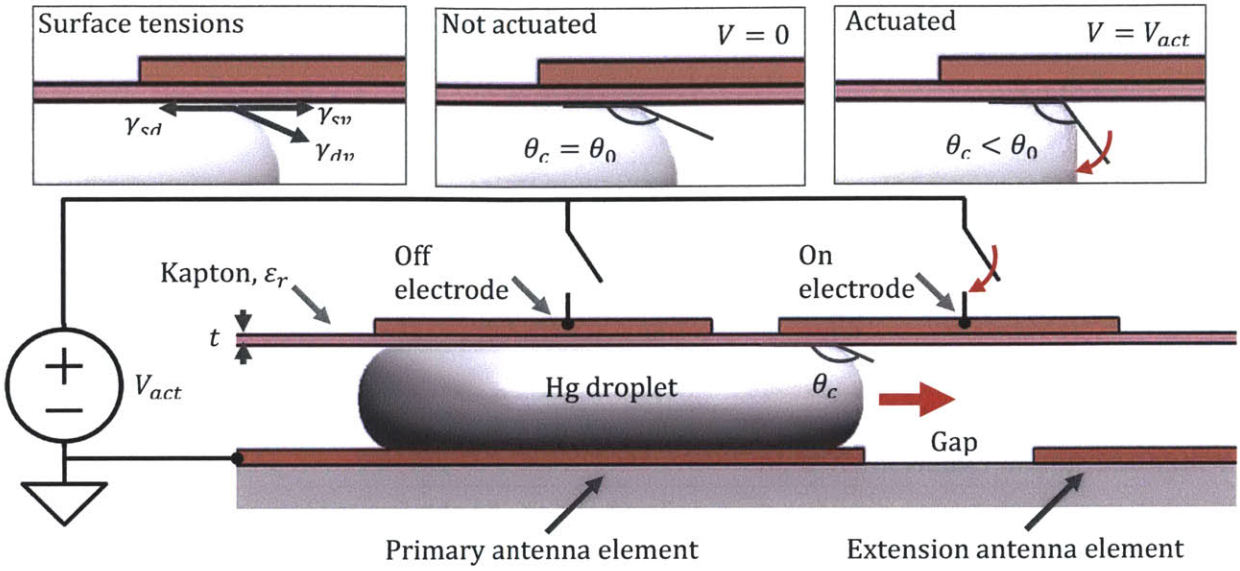

Figure 3.14: Cross section view of electrostatic microswitch

The theory behind EWOD has traditionally been described as a modulation of a droplet's contact angles by an applied electric field. This contact angle perspective is helpful because it explains phenomena observable in most EWOD systems and is couched in the same terms as those used in the preceding analysis of the fluidically actuated switch. The premise is that contact angle modulation creates an imbalance in surface tension forces at droplet interfaces, resulting in a net force on a droplet. Consider the two-plate EWOD setup illustrated in Figure 3.14. The contact angle θ_c of the droplet is governed by the force balance related by the Young equation given by

$$cos(\theta_c) = \frac{\gamma_{sv} - \gamma_{sd}}{\gamma_{dv}}. \tag{3.6}$$

γ_{sv}, γ_{sd}, and γ_{dv} are the interfacial tension between solid-vapor, solid-droplet, and droplet-vapor interfaces, respectively. For this theoretical treatment of the proposed switch, the vapor can be considered air. The solid interface of interest is the dielectric surface, and the droplet is mercury. The original Lippmann equation given in (3.7) relates the change in an interfacial tension to an applied voltage V across a per-unit-area capacitance C' at the interface. In the case illustrated in Figure 3.14, the altered interface is between the mercury droplet and the dielectric surface. Therefore, the solid-droplet interfacial tension γ_{sd} is the applicable surface tension component.

$$\frac{\partial \gamma_{sd}}{\partial V} = -VC' \tag{3.7}$$

The per-unit-area capacitance is $C' = \varepsilon_0 \varepsilon_r t^{-1}$, where ε_0 is the permittivity of free space and $\varepsilon_r$is the relative permittivity of the dielectric film with thickness t. Therefore, (3.7) reduces to a net change in the surface tension at the solid-droplet interface due to a capacitive force per unit length as given by

$$\Delta\gamma_{sd} = -\frac{\varepsilon_0 \varepsilon_r}{2t} V^2. \tag{3.8}$$

Applying this result of the Lippmann equation to the Young equation in (3.6) yields the Young-Lippmann equation given by

$$cos(\theta_c) = \frac{\gamma_{sv} - \gamma_{sd}}{\gamma_{dv}} + \frac{\varepsilon_0 \varepsilon_r}{2t\gamma_{dv}} V^2 = cos(\theta_0) + \frac{\varepsilon_0 \varepsilon_r}{2t\gamma_{dv}} V^2. \tag{3.9}$$

θ_0 is the contact angle without any applied voltage. The rightmost term in (3.9) is referred to as the dimensionless electrowetting number η, which represents the ratio of electrowetting to surface tension forces in a system.

$$\eta = \frac{\varepsilon_0 \varepsilon_r}{2t\gamma_{dv}} V^2 \tag{3.10}$$

The Young-Lippmann equation can be used to determine a net surface tension force due to an applied voltage from modulated contact angles, or it can be recognized that a per-unit-length force is already available from the negative of (3.8). The total force F_e on the droplet is given by (3.11), where W is the length of the contact line over the actuating electrode.

$$|F_e| = W\gamma_{dv}(cos(\theta_c) - cos(\theta_0)) = \frac{W\varepsilon_0 \varepsilon_r}{2t} V^2 \tag{3.11}$$

The preceding contact angle approach to EWOD is somewhat distracting due to its focus on contact angles and surface tensions between the droplet, vapor, and solid. The contact angle approach also presupposes that contact angle difference is necessary for droplet movement, when, in fact, contact angle modulation is only an observable consequence of electromechanical force. Actuation has been demonstrated without observable contact angle changes [31]. Lastly, the above approach cannot explain frequency dependent or dielelectrophoretic behavior [31] that has been demonstrated in some EWOD systems. However, for highly conductive liquid metal droplets such as those under consideration, neither of these effects is of interest.

It is worth noting that an electromechanical approach to EWOD is more generally applicable to electrostatic droplet actuation. It also has the virtue of being more direct than the contact angle electrowetting approach. Reconsider the two-plate setup re-illustrated in Figure 3.15.

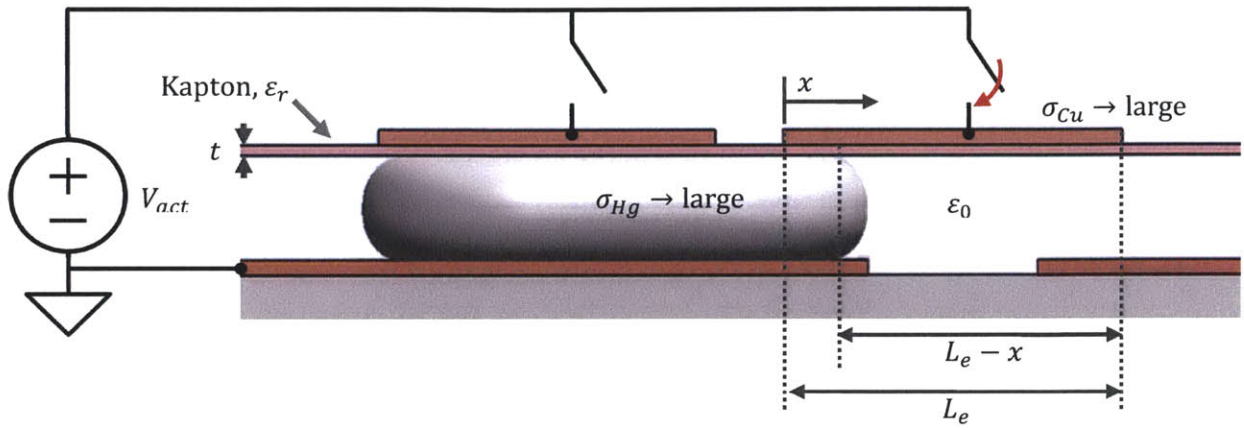

Figure 3.15: Electrostatic microswitch, electromechanical analysis

The capacitive coenergy E' of the system can be approximated as a function of frequency and position given by

$$E'(f,x) = \frac{1}{2}C(f,x)V^2 \tag{3.12}$$

where C is the capacitance of the system bounded by the actuating electrode and the reference electrode; x represents the position of the advancing contact line along the x-axis as illustrated in Figure 3.15. Generally, the capacitance is a function of frequency due to the frequency dependence of fluid permittivities. If the droplet contact line is approximated as a straight line of length W, then the coenergy described in (3.12) can be written as

$$E'(f,x) = \frac{W\varepsilon_0}{2}\left(x\sum_i \frac{\varepsilon_{r,i}(f)}{t_i}V_i^2 + (L_e - x)\sum_j \frac{\varepsilon_{r,j}(f)}{t_j}V_j^2\right), \tag{3.13}$$

where $L_e$is the length of the actuating electrode; $\varepsilon_{r,i}$ and V_i are the relative permittivity and voltage drop across the ith layer in the region where the droplet is present; $\varepsilon_{r,j}$ and V_j are the relative permittivity and voltage drop across the jth layer in the region where the droplet is not present. For the system depicted in Figure 3.15, the dielectric film is the only layer of interest in the region where the droplet is present. Due to its high conductivity, the mercury droplet can be considered grounded by the bottom electrode. In the region above

the actuating electrode without mercury, the layer formed by the vapor phase must be considered in addition to the dielectric film. By differentiating with respect to x, the electromechanical force F_{em} is obtained as

$$F_{em} = \frac{\partial}{\partial x} E'(f,x) = \frac{W\varepsilon_0}{2}\left(\sum_i \frac{\varepsilon_{r,i}(f)}{t_i} V_i^2 - \sum_j \frac{\varepsilon_{r,j}(f)}{t_j} V_j^2\right). \tag{3.14}$$

In the approximation that the contribution of the coenergy in the region without mercury is very low, (3.14) for the system under consideration reduces to

$$F_{em} = \frac{W\varepsilon_0}{2}\sum_i \frac{\varepsilon_{r,i}(f)}{t_i} V_i^2 = \frac{W\varepsilon_0\varepsilon_r}{2t} V^2, \tag{3.15}$$

which is equivalent to the force approximated by the contact angle method in (3.11). This approximation is acceptable for the proposed microswitch because the fluidic layer of the switch is expected to be on the order of 100μm thick with the permittivity of air whereas the dielectric film is expected to be on the order of 1–10μm thick with a relative permittivity ε_r near 3–5. Therefore, the capacitance of the dielectric film will be the dominant contribution to the actuating force, and either the simplified contact angle or electromechanical models for electrowetting can be applied to the proposed microswitch.

Of course, the electromechanical force must exceed surface tension forces and friction to achieve actuation. These forces are somewhat difficult to characterize and are dependent on the particular surfaces involved. As the exact natures of these surfaces are determined not only by material parameters, but also by the fabrication process, an experimental approach is best suited to determine the requirements for actuation.

Despite this hindrance to further useful theoretical analysis, the preceding discussion allows for an estimate of the voltages required for actuation. Mercury exhibits a natural contact angle of 130–150° on most surfaces and a surface tension around 0.4N/m. Since typical EWOD systems exhibit contact angle changes near 20–40° during actuation, a conservative contact angle change of 50° can be targeted as a model actuation requirement. Taking dielectric thickness and permittivity as variables, (3.9) can be solved to estimate the required actuating voltage. Estimates based on a target contact angle change of 50° and an initial contact angle of 140° are plotted against permittivity and thickness in Figure 3.16.

As expected, minimum actuating voltage scales proportionally with the square root of the thickness of the dielectric film and inversely with square root of the film permittivity. Although the required voltage can be reduced by minimizing the film thickness, a limit on

film thickness is imposed by the dielectric strength E_{max} of the material. Breakdown voltage V_{bd} as given by

$$V_{bd} = \frac{E_{max}}{t} \tag{3.16}$$

scales inversely with film thickness. If breakdown voltage is less than actuating voltage, the dielectric film will fail before actuation can be achieved.

In this work, the film thickness was also constrained by resources available for fabrication. Since non-cleanroom processes were favored in this design, a lower limit to practical thickness of the dielectric layer is set by the thicknesses of available dry films. The thinnest widely available dry films are 12.5μm thick. Unfortunately, such a large thickness implies that large actuating voltages will be required. For a 12.5μm Kapton film ($\varepsilon_r = 4, E_{max} =$ 118MV/m) such as one that might be appropriate as a cover for a fluidic switch, the estimated minimum actuating voltage is around 400Vrms. Although below the breakdown voltage, this high actuating voltage is far from ideal. A thinner polyimide layer applied by spin-coating would be preferable in order to lower voltage requirements and should be considered in any future work relating to this switch. Actuating and breakdown voltages for Kapton are plotted against thickness in Figure 3.16(b).

Due to the magnitude of the predicted actuating voltage, an AC excitation was chosen for the electrostatic switch. As mercury is highly conductive, it is expected that at relatively low frequencies on the order of 1kHz, the preceding electrowetting model will apply. AC voltages can be stepped up using signal transformers to achieve the necessary voltage. Since a large current is not required for actuation, the AC-voltage transformer solution is easier than supplying a high voltage DC source. Of course, the effective DC magnitude of an AC voltage is its RMS magnitude. Therefore, when applying the preceding equations, the RMS voltage must be used.

The lateral geometry of the switch is dictated by the desired droplet contact area and the surface tension and friction forces that would allow for bistable switch operation. Based on demonstrated bistable operation of the fluidic switch without any constriction, no constriction was designed for the electrostatically actuated switch. The electrodes should be sized smaller than the contact area of the switch, and the gap between the electrodes should be minimized in order to ensure that the droplet will be exposed to strong electric fields from an adjacent energized electrode. Since the droplet is expected to span a gap of 250μm on the antenna layer, the diameter of its contact area is expected to be at least three times that size or 750μm. Electrodes were dimensioned as squares with a side length of 500μm. The minimum gap between electrodes is limited by the fabrication method. In the case of milling, a gap of 100μm can be expected.

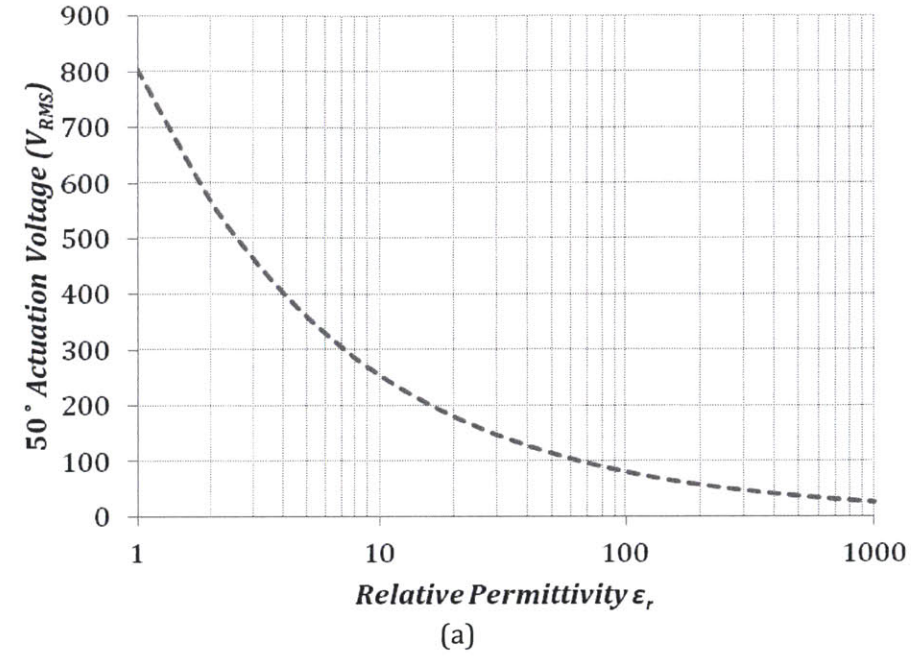

(a)

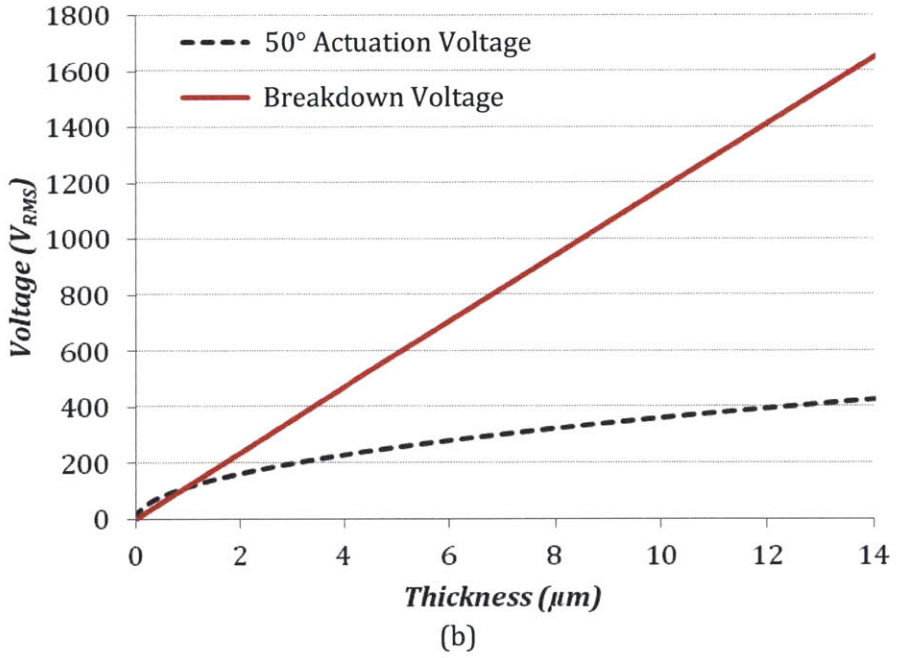

(b)

Figure 3.16: Estimated 50° actuation voltage requirement versus (a) permittivity with film thickness of 12.5μm and (b) versus film thickness with relative permittivity $\varepsilon_r = 4$. Breakdown voltage for Kapton with dielectric strength of $E_{max} = 118\text{MV/m}$ is plotted versus thickness in (b).

Finite-Element Model Simulation

To assist electrostatic switch design, a finite-element model time domain simulation was conducted in COMSOL using the two-phase flow module. A time dependent contact angle boundary condition is imposed under the right electrode to simulate actuation. A complete electromechanical model was not developed because the size of the multi-module simulation was consuming an inordinate amount of time and computation resources. Friction forces are neglected in the model, but the model verifies the principles of operation for the electrostatic switch. The model geometry is shown in Figure 3.17.

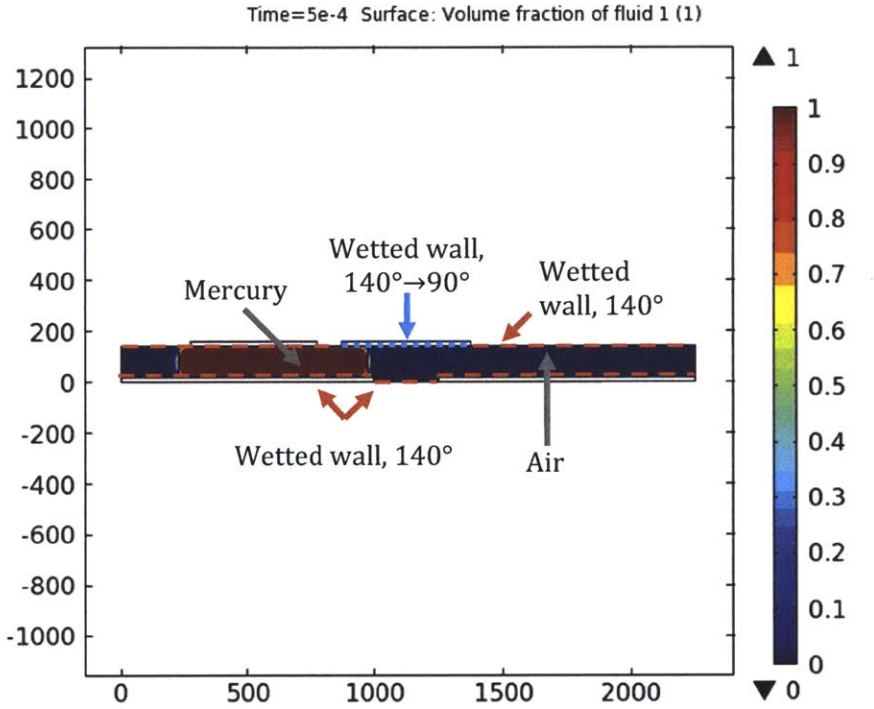

Figure 3.17: COMSOL electrowetting simulation of electrostatic microswitch

The switch height was set to 125μm in keeping with the thickness of the layer used in the fluidic switch. Since an electrostatic force is not modeled, the Kapton layer is omitted to easier define the regions under the electrodes. The channel boundaries were assigned wetted wall conditions with contact angles of 140° except for the boundary under the right electrode, which was assigned an initial contact angle of 140° and changed to 100° after 2ms. The assumed surface tension of mercury in air was 0.4N/m. A mobility tuning parameter of 0.05m/s was used.

The droplet predictably moved from left to right in response to the actuating voltage applied to the right electrode as shown in Figure 3.18. This numerical simulation reinforces the concept of contact angle change as a measure of actuation.

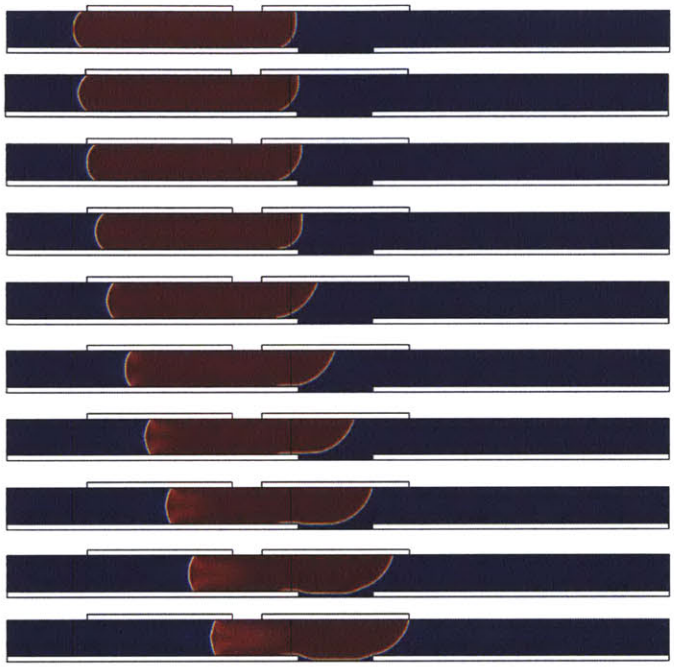

Figure 3.18: COMSOL time domain simulation results for electrowetting model of electrostatic microswitch shown in time increments of 0.5ms after actuation

Fabrication

Prototypes of the proposed electrostatic microswitch were constructed using a process similar to that used in the fabrication of the fluidic microswitch. In this case, two primary prototype versions were created. One version uses solid electrodes printed on the cover layer, and the other has no electrode features on the cover and is intended for use with a movable liquid electrode. The liquid electrode version requires a stylus to manipulate the droplets of electrolyte solution used for the liquid electrodes. This stylus features a metal probe with a capillary tip that uses capillary action to control the electrolyte droplet. In the absence of the capillary tip, an energized electrolyte droplet cannot be manipulated but will rather align with the grounded mercury droplet below it. Illustration of the prototype versions are shown in Figure 3.19. Dimensions are summarized Table 3.2. A milled slot is used for lateral containment of the droplet in both cases. More solid electrodes are included than strictly required to minimize the impact of any misalignment. Also, the slot is enlarged in the shown prototypes so that actuation is more clearly visible. Other prototypes with a smaller slot were also constructed and demonstrated successfully.

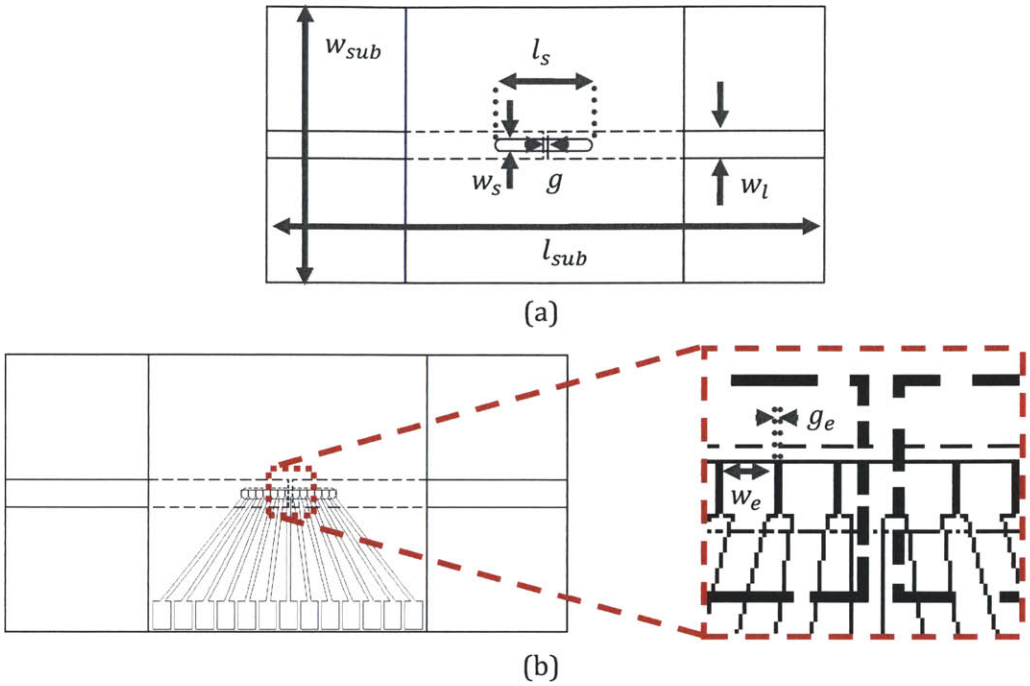

Figure 3.19: Layout of prototype electrostatic switches with (a) liquid and (b) solid electrodes.

Table 3.2: Dimensions of prototype fluidic switch

w_{sub}	l_{sub}	w_l	w_s	l_s	w_e	g_e	g
20mm	40mm	2.6mm	800µm	2.5mm	500µm	30µm	250µm

Versions of the switch with additional evaporated 0.5µm platinum or 0.1µm gold and 0.5µm nickel on the original copper traces were also constructed in order to compare contact resistances of different solid metal-mercury combinations. Platinum does not amalgamate with mercury, and even though gold does, it was hoped that conductivity might actually be improved by the amalgamation process and that the nickel would remain fairly stable. However, completed prototypes with evaporated gold and nickel on copper proved extremely unstable, with the mercury quickly wetting the gold surface and spreading into a thin film on its surface. This film even reacted with gold underneath and beyond the fluidic layer adhesives as shown in Figure 3.20.

The fabrication process for the electrostatic switch prototypes was based on that developed for the fluidic switches and was conducted as follows:

1. Platinum or nickel and gold layers were evaporated onto electroplated copper on a TMM10i. Some versions of the switch did not include this evaporation step in order to have purely copper traces for comparison. Versions used only for actuation testing were constructed using only copper on FR4 and also excluded this step.

2. The circuitry of the switch was milled using a PCB milling machine.

3. 3M467 double-sided adhesive transfer tape was applied to both sides of the 5mil Kapton fluidic layer material under 50psi pressure for 1min.

4. The Kapton fluidic layer material and attached adhesives were milled together on a PCB milling machine to form the channel outlines.

5. The Kapton fluidic layer was then attached to the circuit board with the adhesive transfer tape tape under 50psi pressure for 1min.

6. For the solid electrode prototype, a 12.5μm AC Pyralux film with single-side plated copper was etched to form the electrodes. The etch mask was made from a coat of black enamel spray paint patterned with a 1mil spot size IR laser milling machine. For the prototype intended for a liquid electrode, an un-plated 12.5μm Kapton film was used as a cover, and no milling was required.

7. A 0.5mg mercury droplet metered by a controlled growth mercury electrode dispenser was placed in the switch. A small amount of silicone oil was added to the switch as a lubricant.

8. The Kapton covers were attached to the prototypes under 50psi pressure for 1min. Solid electrode covers were first attached with transfer tape to a 10mil plastic cover and then attached to the switch in order to flatten the surface of the cover. The solid electrode covers would curl up without first attaching them to a flat surface.

9. The stylus for liquid electrode manipulation was constructed from a blunt multimeter probe and a plastic pipette tip cut to form an entry diameter of 2mm.

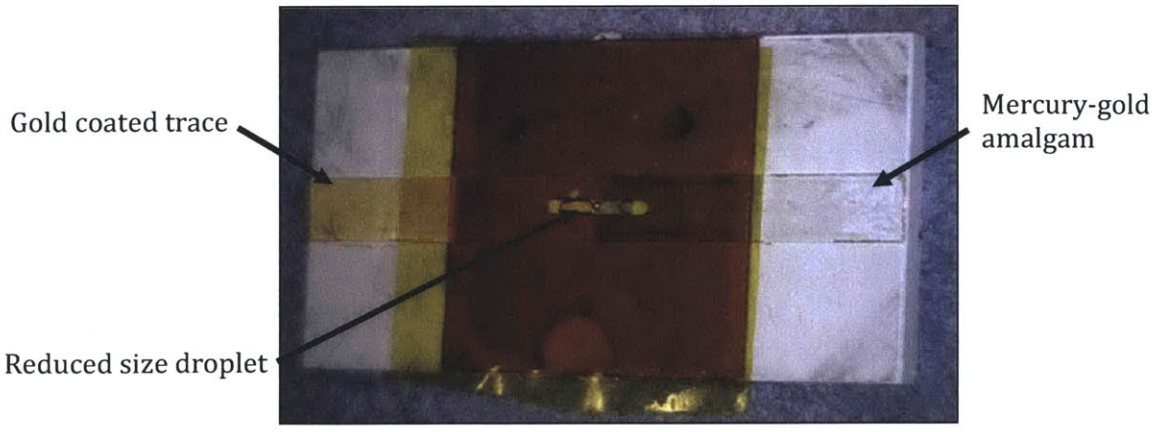

Figure 3.20: Amalgamation of mercury onto gold-coated prototype

Photographs of electrostatic switch prototypes are shown in Figure 3.21. Two of the structures are designed with larger slots than necessary for clear actuation demonstration. Switch prototypes with SMA connectors were used in switch characterization. Test structures without switch features were also constructed using the above process. Silicone oil was not included in the initial process, but experiments on both the test structures and switch prototypes showed that silicone oil was necessary to ensure reliable droplet actuation at voltages below 900Vrms. These observations will be discussed in more detail in the following section.

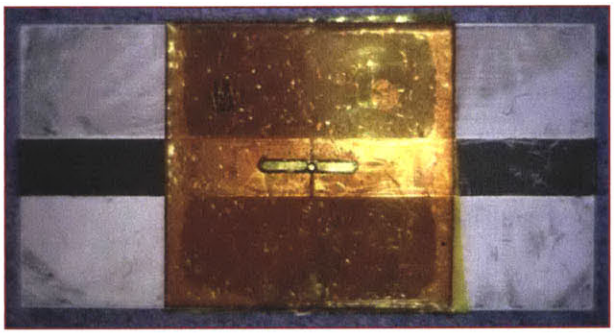

(a)

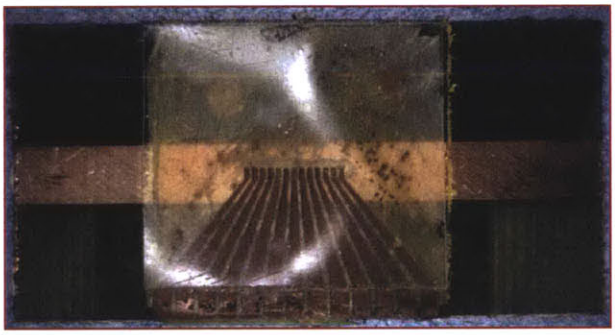

(b)

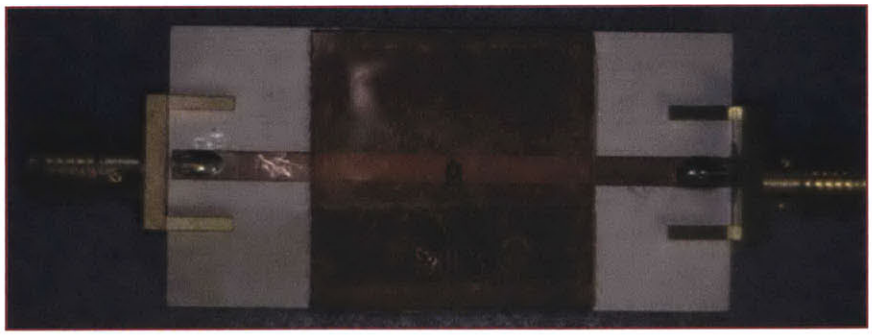

(c)

Figure 3.21: Electrostatic switch prototypes for demonstration with (a) liquid electrodes and (b) solid electrodes. (c) Prototype for RF characterization with solid electrodes.

Measurements

A number of experiments were conducted on open test structures before the switch prototypes were conducted in order to validate actuation. Frustratingly, the droplet did not actuate even for voltages as high as 860Vrms. Voltages were obtained by step up with a 1:122 turn ratio signal transformer. A 100nm fluoropolymer was deposited on the test structure to the decrease the contact area of the droplet on the bottom grounding plane. Unreliable actuation was observed even under these conditions.

A solution to this actuation problem was found by applying silicone oil to the bottom surface of the structure. The silicone oil appeared to have a lubricating effect on the mercury droplet, and actuation was achieved reliably at voltages between 600-700Vrms. The exact voltage was not characterized because a sufficiently large attenuator was not available to observe the waveforms on an oscilloscope. Images from a video recording of actuation in the test structure using a liquid electrode are shown in Figure 3.25.

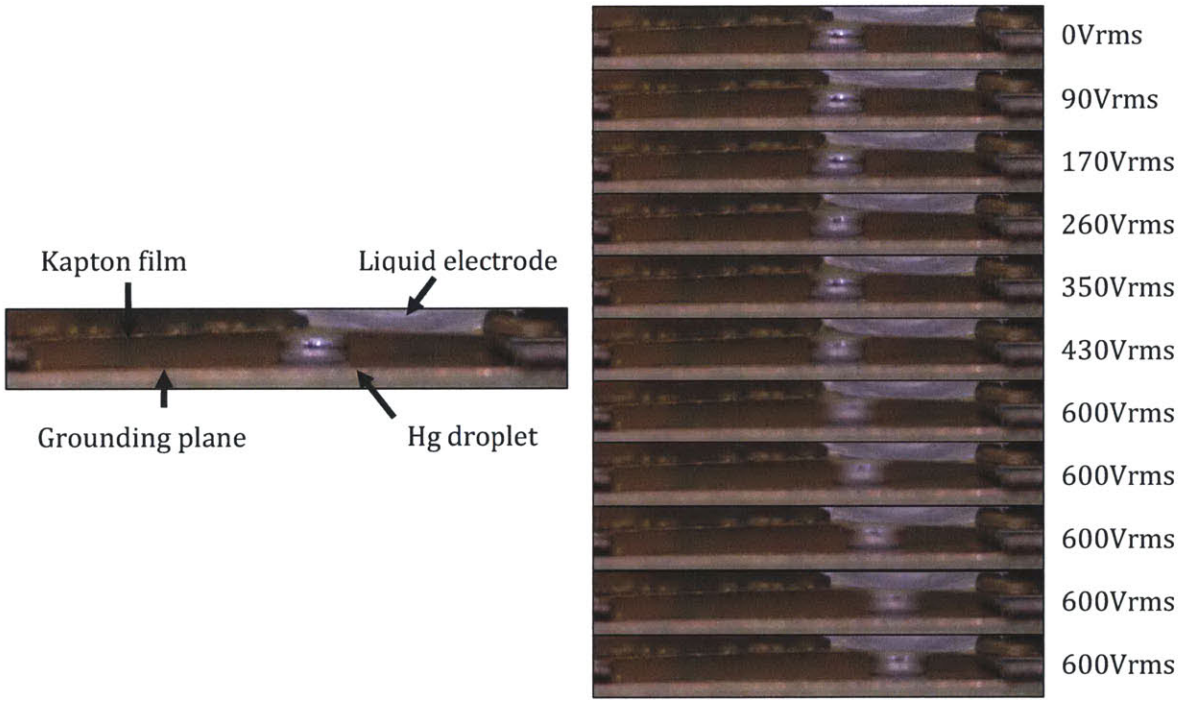

Figure 3.22: Video captures of mercury droplet actuated by liquid electrode with increasing applied voltage from 0-600Vrms. Observable actuation first occurs at 600Vrms.

Both liquid and solid electrode switch prototypes successfully actuated. Images from video recordings of actuation using both liquid and solid electrode prototypes are shown in Figures 3.26 and 3.27, respectively. The liquid electrodes offer greater flexibility and droplet control than solid electrodes but must be manually controlled and cannot be practically integrated into a complete system.

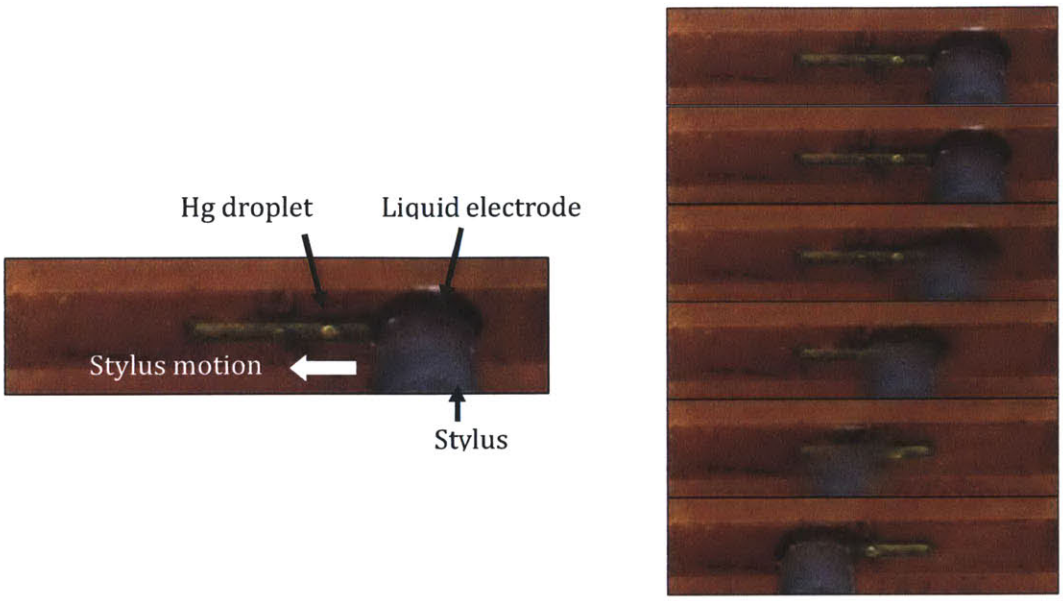

Figure 3.23: Image captures from video of liquid electrode prototype actuation under 860Vrms applied via stylus moving from right to left; increasing time from top to bottom.

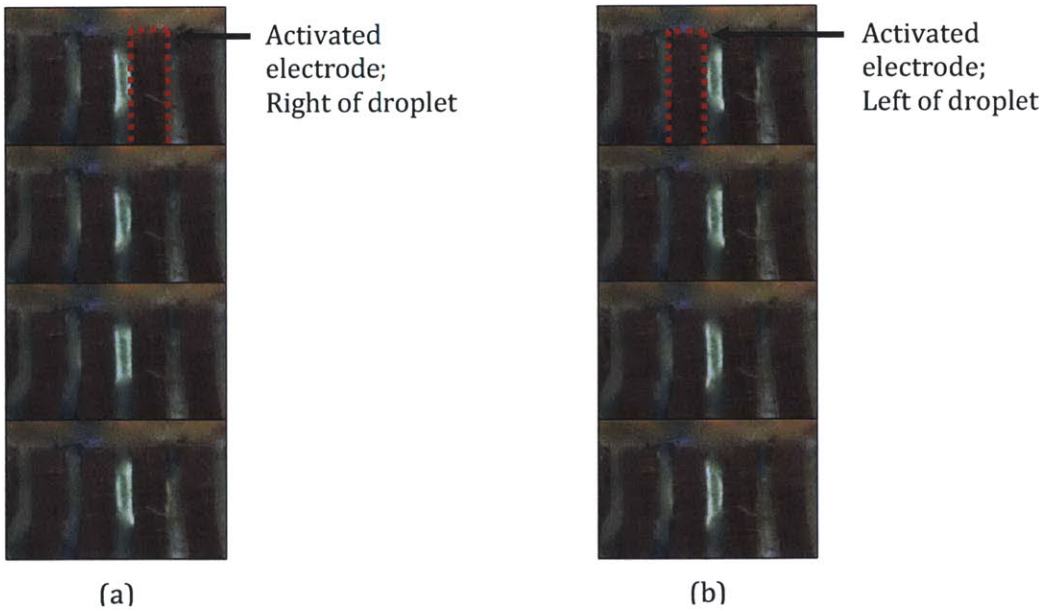

Figure 3.24: Solid electrode prototype actuation under 860Vrms applied in sequence to electrodes from (a) left to right and (b) right to left; increasing time from top to bottom

Static ohmic resistance of the switches in the on-state was measured using a 4-point technique with an Agilent 34401A digital multimeter. The average on-state resistance was 42mΩ for copper switches and 33mΩ for platinum switches. Isolation and insertion loss of the switch prototypes were measured with an Agilent E8363B network analyzer. The results indicate isolation better than 10dB up to 3GHz in the off-state and an insertion less than 1dB up to 4.5GHz in the on-state for all configurations as shown in Figure 3.29. Again, the switch structure is not directly representative of the actual insertion loss or isolation seen in any specific patch antenna geometry, but the general operation of the device as an RF switch at the frequencies of interest is verified by the measurements. In general, the isolation of the solid electrode switches is better than the liquid electrode versions at higher frequencies, but the insertion loss of the solid electrodes is worse than that of the liquid electride versions at higher frequencies. However, these frequencies are not of interest of the intended antenna application.

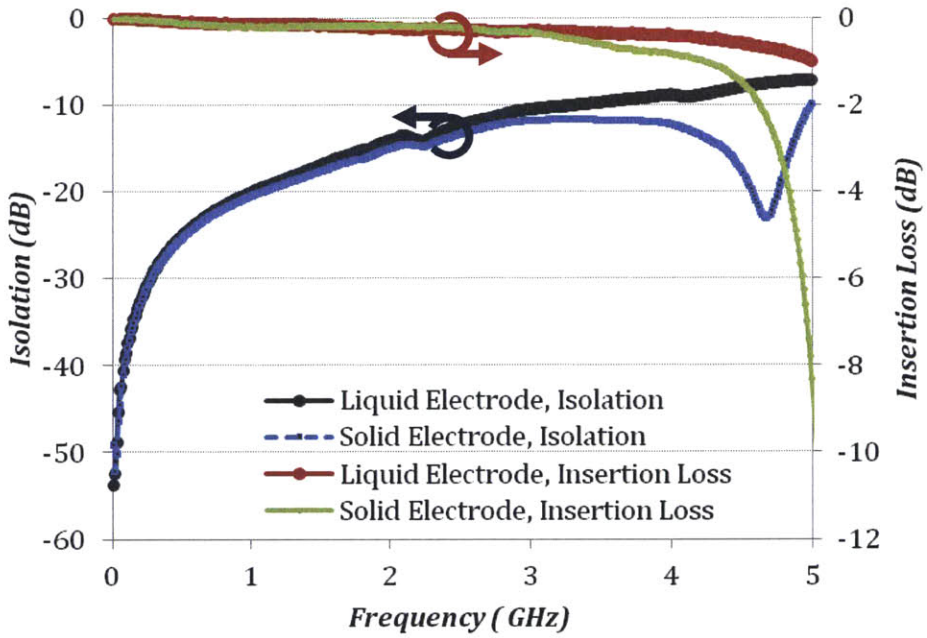

Figure 3.25 Isolation and insertion loss of solid and liquid electrode microswitch prototypes

As expected, bistable operation was observed for the switch despite lacking any constriction. Switches were held at various angles and no droplet translation was observed. Actuation was not always successful in both directions with the solid electrode prototypes, which required precise positioning of the electrodes in order that the mercury droplet be exposed to fields from both electrodes. Sometimes the droplet would move under the first actuated electrode and was thereafter unable to be actuated in the opposite direction. This difficulty points to the need for further optimization of the slot and electrode dimensions.

3.4 Summary and Comparison

Designs for two different liquid metal switches based on fluidic and electrostatic actuation, respectively, have been presented. A summary of the development of each switch type and their respective attributes are summarized in Table 3.3.

Table 3.3: Comparison of fluidic and electrostatic switch designs

	Fluidic	Electrostatic, Liquid	Electrostatic, Solid
Resistance	43mΩ,Cu	43mΩ, Cu; 33mΩ, Pt	60mΩ, Cu
Actuation Achieved	No	Yes	Yes*
Control	Electronic, pump	Electronic, voltage	Electronic, voltage
Actuation Requirements	Pump, high voltage	Stylus, high voltage	Electrode, high voltage
Integration Requirements	Manifold, valves	No integration	Electrode network, transformer
Fundamental Disadvantages	Central actuation, difficult scaling	No integration	RF parasitics
Further Work	Process development, stronger pumps	None	*Optimize slot and electrode dimensions

The fluidic switches were analyzed and fabricated but were not successfully actuated due to excess friction and the lack of a controllable source of sufficient pressure for actuation. Also, many devices suffered from leakage. These issues can be addressed by a more precise and robust fabrication process and experimental fluidic testing. The fluidic structures should be defined either by photolithography or through UV laser milling to obtain smoother side walls. This should reduce friction within the channel. More alternative low temperature adhesives should be explored to provide a more robust seal to the devices. An experimental approach to determining the required actuation pressure should be pursued using a macroscale pump. Although this could have conceivably been applied to the constructed prototypes described here, it should be noted that silicone oil is very difficult to remove. A dedicated pump would be needed, likely at large financial cost. It appears that alternative actuation methods are more promising.

Electrostatic switches presented as an alternative to fluidic actuation were analyzed, fabricated, and successfully actuated. Although droplet actuation was achieved using both liquid and solid electrodes, it should be noted that the solid electrode version of the switch requires further optimization. Compared to the liquid electrode version, the solid electrode switches require precise dimensioning and alignment of the electrodes to the droplet and

control of droplet contact area. Many of the constructed prototypes demonstrated initial actuation, with the mercury droplet moving under the first actuated electrode, but the droplet sometimes could not be subsequently actuated in the reverse direction because the contact area of the droplet did not see sufficiently strong electric fields from the second electrode. The current process does not allow for very precise control of alignment or minimization of the gap between actuating electrodes. Minimizing the gap between electrodes and increasing the electrostatic force magnitude with a thinner dielectric film could solve these issues that result in low device yield for the solid electrode switches. Like the fluidic switches, the electrostatic switches would likely benefit from smoother channel side walls obtained through photolithographic or UV laser milling methods. These improvements are certainly feasible and should be pursued as the next steps in the development of the solid electrode microswitches.

The experiments conducted with constructed prototypes clearly indicate that electrostatic microswitches are more promising than fluidic ones based on successful actuation in the former and not in the latter. But even assuming that the fluidic switch could be actuated successfully, the electrostatic actuation method would still be preferable for integration with a reconfigurable patch antenna based on its qualitative advantages. Although both methods could result in a low resistance, controllable microswitch, fluidic actuation faces more difficult system level problems than electrostatic actuation does. These challenges are not only technological, but also topological in nature. The technological problem with fluidic actuation is that compact bidirectional pumps capable of liquid flows on the order of mL/min and kPa of backpressure are possible but not readily available. Such pumps may also impose demanding electrical requirements similar to those associated with electrostatic actuation. For example, the unidirectional piezoelectric micropump used to evaluate the proposed fluidic switch could not actuate the prototype switch even with driving voltages as high as 250Vrms.

The topological issues surrounding fluidic actuation are more serious. Even in the case that a suitable pump can be found, that pump must serve as the pressure source for multiple switches acting in parallel. It is even probable that multiple sets of switches must be actuated independently. Therefore, a complex manifold system must be designed. Such microfluidic piping introduces time delays in the switching process. The control situation becomes even more problematic if these time delays are non-uniform. Fluid flow also presents the increased possibility of leakage, which constitutes not only device failure, but also a safety hazard when the working fluid is contaminated with mercury.

By contrast, the proposed electrostatic method uses localized forces that allow for independent operation of multiple switches with minimal flow, thus minimizing the chance of leakage. The main system level challenge facing electrostatic actuation is the high voltage requirement. However, it has been shown that this voltage can be reduced with thinner

high permittivity films possible through other fabrication processes. In fact, similar EWOD-based systems have demonstrated actuation with voltages as low as 20V [30]. The high voltage required for the presented microswitches reflects circumstantial limitations surrounding fabrication resources as opposed to fundamental ones. The one significant fundamental drawback of electrostatic actuation is the parasitic presence of control electrodes. However, it is highly probable that any parasitic effects can be compensated by appropriate antenna design. Based on its scalability and eminently solvable disadvantages, electrostatically actuated switches were selected over the fluidic switches for integration with a frequency and polarization reconfigurable patch antenna. The design of that antenna and its integrated switches is the subject of the next chapter.

Chapter 4

A Reconfigurable Microstrip Antenna

4.1 Specifications

A compact frequency and polarization reconfigurable single-feed circularly polarized patch antenna is presented as an application of the proposed microswitch. This application demonstrates wide reconfigurability in a compact form factor but is only one of many potential applications for the proposed microswitches. The antenna is designed to switch between three modes: right-hand circularly polarized (RHCP) operation at the GPS frequency of 1575MHz and left-hand circularly polarized (LHCP) operation at both the Advanced Wireless Services (AWS) downlink band centered on 2132.5MHz and the industrial, scientific, and medical (ISM) band centered on 2450MHz.

The antenna is limited to a $10.25cm^2$ footprint and a thickness of 110mils, constraints consistent with compact applications. A single feed is specified in order to avoid additional insertion loss by switching between hybrids. Target gain is greater than -6.4dBic at 80° off boresight as measured on a circular 4inch diameter standard ANSI ground plane.

The antenna is initially designed using electrostatic microswitches with liquid electrodes. Because the liquid electrode configuration presents a minimal parasitic load to the antenna, it allows more straightforward design of the underlying topology of the antenna. Moreover, liquid electrode actuation proved the more robust of the switch prototypes. However, the liquid electrode actuation method is not suitable for integration, and the effect of the parasitic effect of a solid electrode cover is characterized as a first step toward an integratable design.

4.2 Principle of Operation

The antenna achieves reconfigurability by band-switching between three modes in a novel topology. The antenna mode is set by 16 microswitches that selectively connect extensions to a truncated corner square patch antenna. The antenna's ISM mode is comprised of only the central truncated corner square patch as illustrated in Figure 4.1(a). The side lengths of the patch are square with the exception of two truncated corners arranged along a diagonal. The side length dimensions generally follow the relations given in (2.4) although the actual lengths are slightly shorter than predicted due to fringing effects. As discussed in Chapter 2, the polarization sense is determined by the feed orientation with respect to the chamfered corners. In this case, the feed is placed such that LHCP operation is achieved.

Axial ratio control is achieved by sizing the chamfered corners correctly. Increased chamfer sizes result in greater asymmetry and, therefore, greater frequency separation of the degenerate antenna modes. This dimension was determined through parameterized simulation as will be discussed in the following section.

The AWS mode is achieved by electrically connecting the patch to the small traces positioned near its corners by means of the liquid metal switches as shown in Figure 4.1(b). The traces extend the electrical length of the antenna, thereby lowering its resonant frequency. Axial ratio control is achieved by sizing the extension trace lengths such that the four traces extending from corners A and D are all 4.825mm in length, and the four traces extending from corners B and C are all 4.925mm in length. The asymmetric lengths allow independent control of the degenerate modes at the AWS frequency and are verified through parameterized simulation. Again, the asymmetries of the traces are oriented for LHCP operation.

The GPS mode is achieved by opening the switches to the small traces at the corners of the square patch and closing the switches connecting the patch to the outer ring as illustrated in Figure 4.1(c). The outer ring approximates a truncated corner patch antenna with the orientation of the corners chosen such that the antenna operates with RHCP. The chamfered corners of the GPS extension are along the diagonal opposite to that along which the chamfered corners of the inner ISM patch are aligned. Again, axial ratio is controlled by the size of the chamfered corners on the GPS extension.

The antenna structures are patterned on a 75mil Rogers TMM10i substrate (ε_r = 9.8). A high permittivity substrate was selected to reduce the antenna area to within a 10.24cm^2 area. The high permittivity substrate reduces the effective wavelength at the GPS frequency to about 61mm, and therefore, half wavelength resonance can be achieved within the designated area constraints. No further efforts are made to miniaturize the antenna in order to preserve as much gain as possible within the footprint requirements.

The antenna is directly fed by a coaxial probe for simplicity. The feed point is chosen near the antenna centerline and oriented with respect to the truncated corners such that the desired polarizations are achieved. The exact feed location is a compromise between the ideal 50Ω feed points for each of the configurations and is verified by parameterized simulation. Although not explored here, alternative wideband feeding mechanisms may be more appropriate for a single feed frequency reconfigurable antenna. Aperture, proximity, and meandered probe are several feeding techniques used to achieve wider impedance matching bandwidth in patch antennas. The impedance bandwidths of antennas using such methods are also generally less sensitive to manufacturing tolerances than those that use coaxial feeds. This topic represents an opportunity for future work.

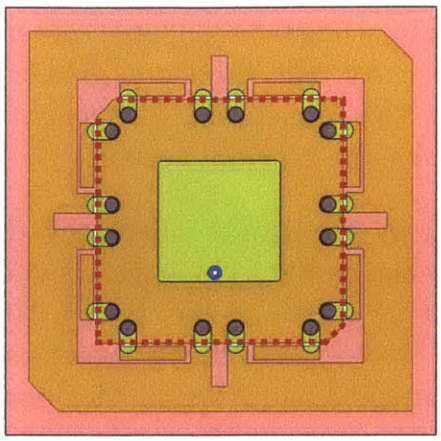

(a)

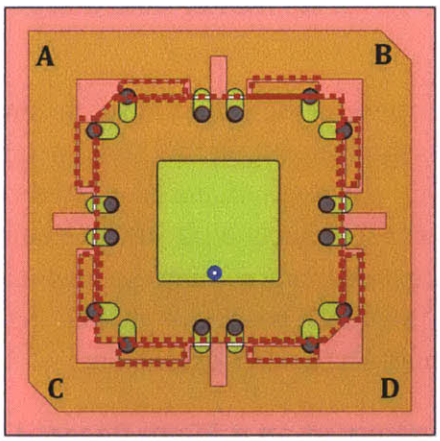

(b)

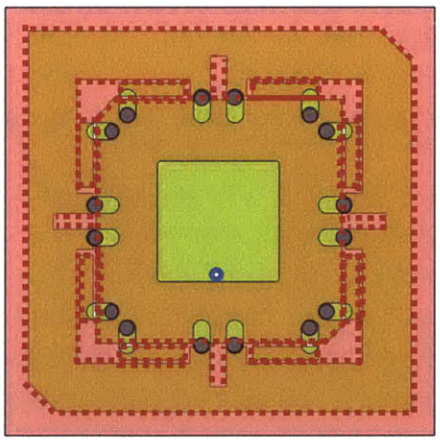

(c)

Figure 4.1: Illustration of (a) ISM, (b) AWS, and (c) GPS configurations. Grey dots represent mercury positions. Active antenna areas are outlined in red. Feed point is marked in blue.

4.3 Finite Element Full-Wave Simulation

The design of the antenna topology is completed using Ansoft HFSS full-wave simulation software. The use of electromagnetic software is useful in determining small, critical dimensions in the antenna such as the size of chamfered corners, extension trace asymmetries, and feed location. The simulation model is shown in Figure 4.2.

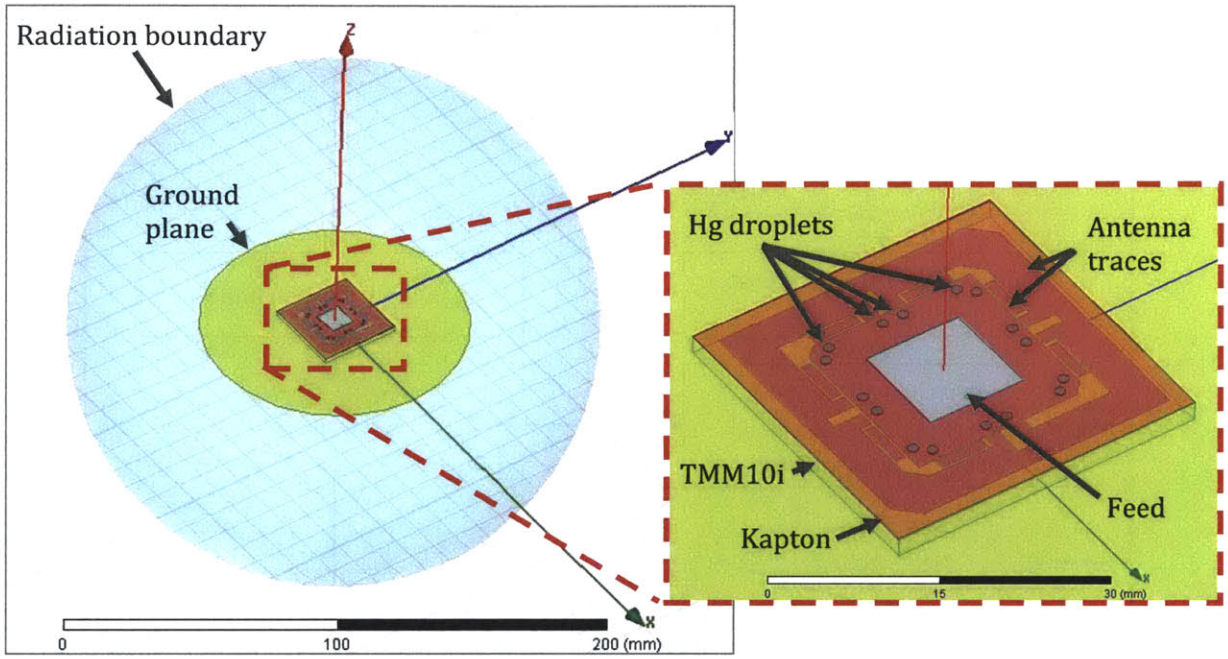

Figure 4.2: HFSS simulation model of three band reconfigurable patch antenna

The simulation models the antenna up to the input end of the probe feed. The model approximates the liquid metal switches as cylinders with the nominal conductivity of mercury, $\sigma_{Hg} = 1 \times 10^6$ S/m. Contact resistance is neglected. To reduce the numerical size of the model, the thin solid antenna traces are modeled as sheets with conductivity of copper $\sigma_{Cu} = 5.8 \times 10^7$ S/m. The simulation is conducted in driven terminal mode, and a spherical radiation boundary with radius $r_{rad} = 100$mm is assigned for far field analysis.

The design and simulation process is completed in an iterative fashion and is summarized in the diagram shown in Figure 4.3. The design process begins with estimates of the required antenna side length dimensions based on formulae given in (2.4) and (2.5) using the selected substrate. Then, the ISM patch, absent any extensions, is modeled based on these estimates. The side length, chamfer size, and feed location for the ISM patch are determined by simulation with these dimensions parameterized until the performance metrics for the ISM band are satisfied.

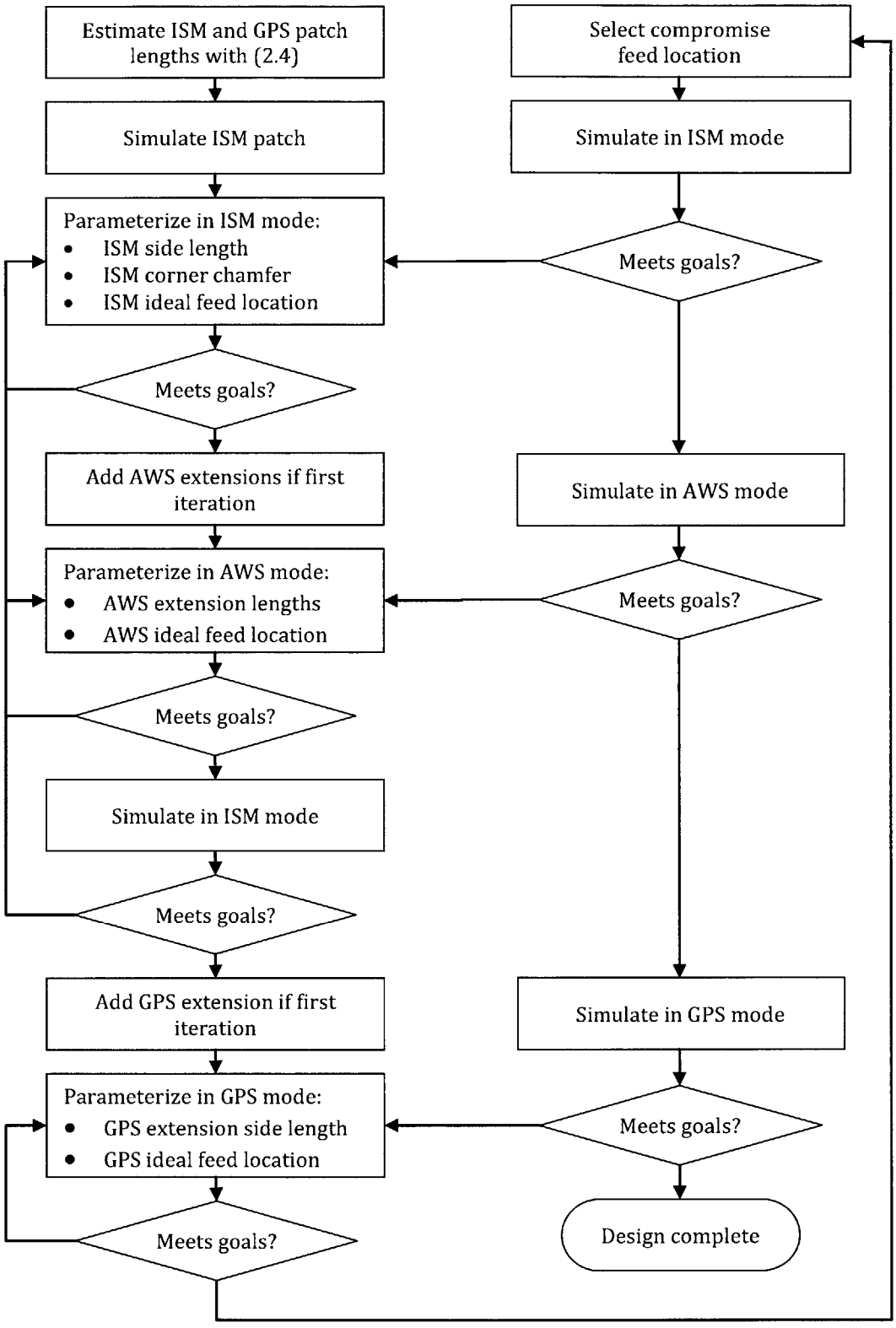

Figure 4.3: Simulation approach to reconfigurable antenna

Next, AWS extensions and their associated switches are added to the model. Starting with the switches set to the AWS mode, the antenna is again simulated, this time with parameterized dimensions for the extensions and the feed location. Swept parameter simulations of the ISM and AWS band configurations without the GPS extension are performed in a loop until performance metrics for both the ISM band and AWS band are simultaneously satisfied with the exception of the feed location. The simulated feed locations are allowed to vary within a small range of ±2mm in order to optimize impedance matching for these preliminary simulations. The final feed location will be determined as a compromise between all three feed locations at the end of the simulation process.

Once the AWS and ISM parameters are dimensioned, the GPS extensions and associated switches are added to the model. Again, a loop is performed, this time performing simulations in all three configurations while still allowing the simulated feed location to move in a small range in order to maintain reasonable impedance matching. Although obtaining desired performance simultaneously would appear difficult when balancing three different modes, the earlier steps using only two modes reduce the number of iterations that need to be performed with all three configurations.

As mentioned in the previous section, increasing asymmetry in the antenna structures results in greater separation of the degenerate modes of the antenna. Therefore, the chamfer and extension dimensions are parameterized to set the axial ratio in the respective bands for which they are connected to the central patch. Illustrative simulation results of the effect of antenna asymmetry are shown in Figure 4.4 on a Smith Chart plot.

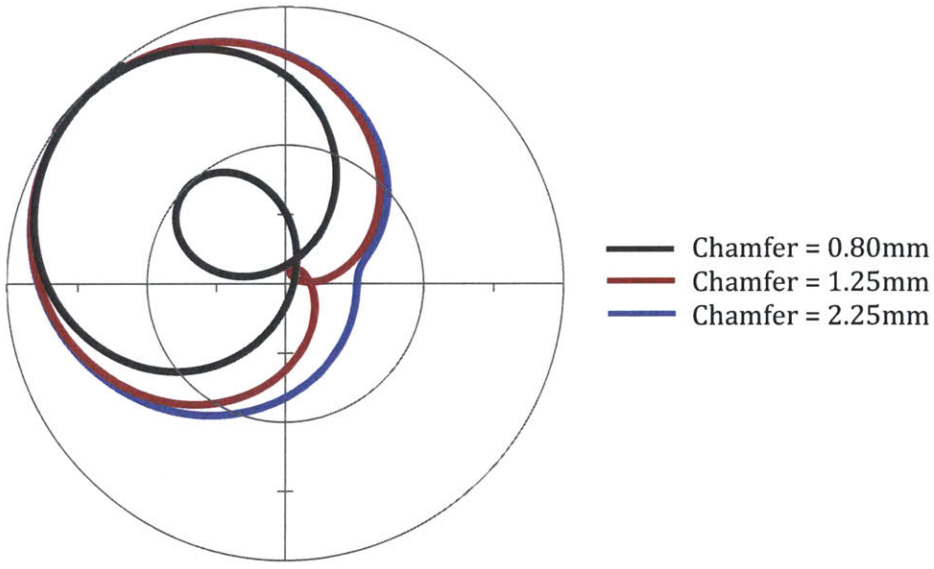

Figure 4.4: Smith chart plot of antenna impedance with parameterized chamfer size

The Smith Chart is an effective tool for visualizing both impedance matching and CP operation in a single plot. The design goal is for the antenna impedance curve to pass through the center of the chart, which represents the normalized 50Ω point, with a small inner loop or dip as illustrated in the red curve shown in Figure 4.4. The small loop is the result of two excited degenerate modes that create a rapidly varying impedance phase as was illustrated in Figure 2.6. Large loops indicate that the antenna has too much asymmetry, and the two degenerate modes are too far apart in frequency for CP operation. The absence of a loop indicates that the antenna is too symmetrical, and no mode degeneracy is achieved.

Once the physical dimensions except for the feed points are determined, the final feed location can be determined by examining how the impedance of each mode varies with feed location. For any given mode at resonance, real impedance increases the closer the feed point is to the edge of the antenna and diminishes near the center of the antenna. This is expected since the electric field distribution of the resonant modes is cosinusoidal in form. For a given feed location, the higher frequency configurations exhibit larger impedances than lower frequency configurations do. This is illustrated in Figure 4.5, which plots simulated real impedance of the ISM, AWS, and GPS modes for a feed located at (-4mm, 0.25mm). Coordinate origin is at the center of ISM square patch neglecting chamfered corners or, alternatively, at the center of the circular test ground plane.

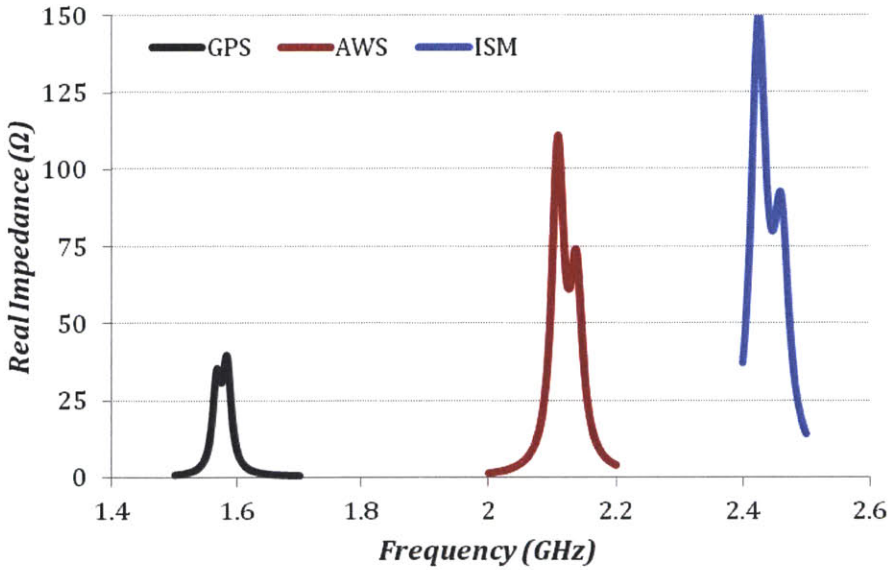

Figure 4.5: Simulated real impedance of ISM, AWS, and GPS mode for a single compromise feed location. Impedance increases for higher frequencies.

As the coaxial feeding technique is rather narrowband, the final feed location is determined as a compromise between the ISM, AWS, and GPS modes. In order to meet performance goals in all three bands, the feed location should be moved from its optimized points for each configuration and averaged to determine a compromise feed point that is not optimal for any single configuration but acceptable for all of them.

4.4 Fabrication

The layout for the constructed antenna prototype is shown in Figure 4.6. Dimensions are summarized in Table 4.1.

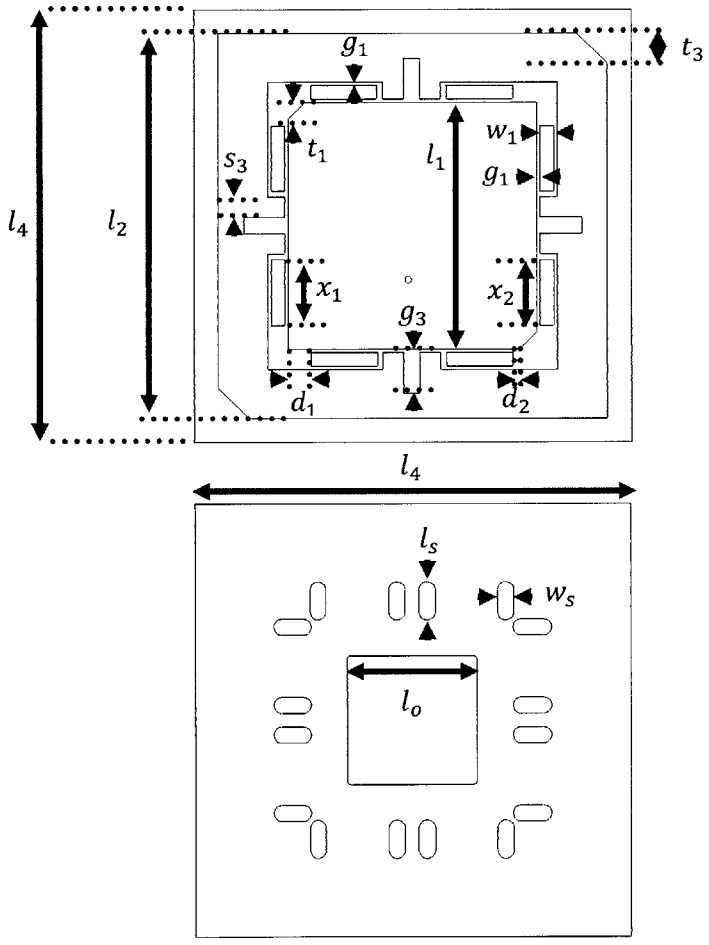

Figure 4.6: Layout of antenna prototype

Table 4.1: Dimensions for prototype reconfigurable antenna

l_1	t_1	d_1	g_1	w_1	x_1	l_2	x_2	d_2	t_3	s_3	g_3	l_s	w_s	l_o	l_4
18.25 mm	1.35 mm	1.75 mm	0.5 mm	1.0 mm	4.875 mm	28.5 mm	4.85 mm	0.4 mm	1.75 mm	1.5 mm	4.25 mm	1.25 mm	0.8 mm	5 mm	32 mm

A layout for the solid electrode cover used to characterize parasitic effects is shown in Figure 4.7. Dimensions are not described because the design of the cover is not optimized and is only intended to be representative of a possible topology for a solid electrode cover for an integratable solution.

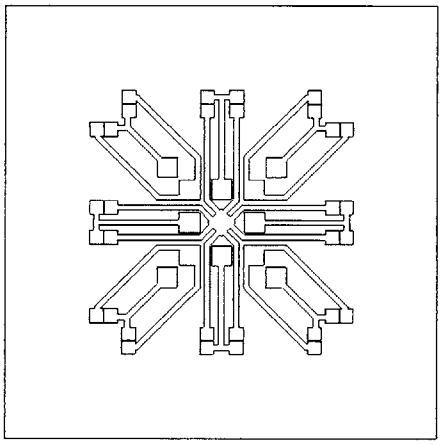

Figure 4.7: Solid electrode cover used to characterize parasitic effects on antenna performance

The described antenna is fabricated using circuit board techniques in a process based on that developed for the electrostatic switch prototypes. The process used in the development of the antenna prototypes is as follows:

1. 0.5μm platinum is evaporated onto copper clad 75mil TMM10i.
2. 3M467 double-sided adhesive transfer tape was applied to both sides of the 5mil Kapton fluidic layer material under 50psi pressure for 1min.
3. The Kapton fluidic layer material and attached adhesives were milled together on a PCB milling machine to form the switch slots.
4. The Kapton fluidic layer with milled slots was attached to the antenna substrate with adhesive transfer tape under 50psi pressure for 1min.
5. For the solid electrode version of the antenna, a 12.5μm AC Pyralux film with single-side plated copper was etched to form the electrodes. The etch mask was made from a coat of spray paint patterned with a 1mil spot size IR laser milling machine.
6. 0.5mg mercury droplets metered by a controlled growth mercury electrode dispenser were placed in the switch slots in two switch pairs. A small amount of silicone oil was added to each switch as a lubricant.

7. The Kapton cover was attached to the prototypes in 8 pieces covering 2 switches each under 50psi pressure for 1min. The cover was attached piece-wise in order to minimize exposure to free mercury during fabrication. In a complete solid electrode prototype, the cover pieces would first be attached to 10mil plastic sheets to ensure a flat surface and aid alignment. However, this step was not conducted in the constructed prototypes, which only used liquid electrodes for actuation.

A photograph of a completed antenna prototype is shown in Figure 4.8. A photograph of a solid electrode cover is shown in Figure 4.9.

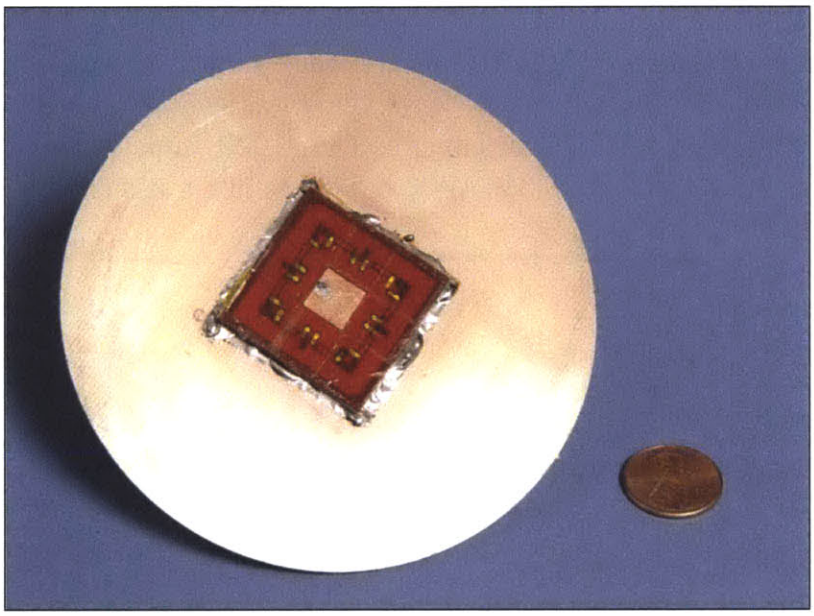

Figure 4.8: Photograph of constructed antenna prototype with test ground plane

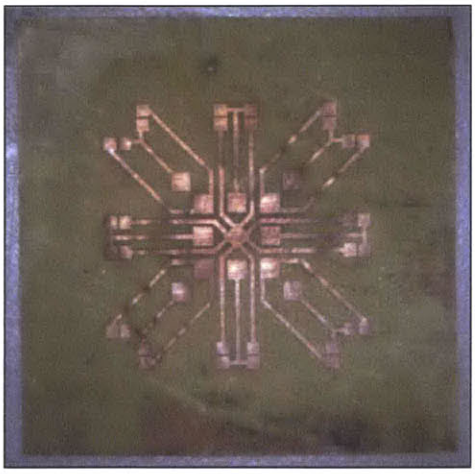

Figure 4.9: Photograph of constructed antenna prototype with test ground plane

4.5 Measurements

The switches of the constructed antenna prototype were successfully actuated using the liquid electrode technique described in Chapter 3. The mercury droplets were grounded through a DC bias on the antenna feed.

The measured and simulated return loss of a prototype antenna in each of its three configurations is plotted in Figure 4.9. The measured resonant frequencies are at 2397MHz, 2091MHz, and 1535MHz for the ISM, AWS, and GPS switch configurations, respectively. These measured resonant frequencies are lower than those predicted by simulation by 2.53%, 1.85%, and 2.22%, respectively. This discrepancy is likely a result of the unmodeled electrical characteristics of the adhesives. However, the reconfigurable frequency of the design is still validated by the measurements. The -10dB impedance bandwidths are 10MHz, 26MHz, and 12.5MHz for the ISM, AWS, and GPS configurations, respectively.

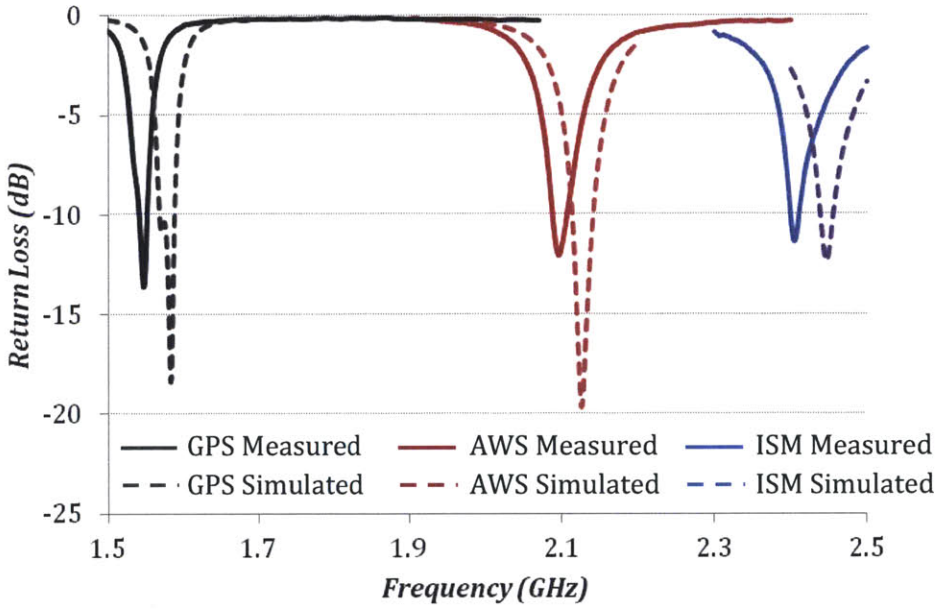

Figure 4.10: Measured and simulated antenna return loss

For the prototype antenna in the ISM mode, a peak gain of 4.9dBic was measured. In the AWS mode, a peak gain of 3.91dBic was measured. In the GPS mode, the peak measured gain is 1.63dBic. This GPS gain was about 2.5dBic lower than expected and is likely a result of higher than expected resistance in some switches. GPS gain was measured at 2.93dBic in a hard-wired version of the antenna.

The minimum boresight axial ratios of the antenna in its ISM, AWS, and GPS modes are 1.43dB, 2.82dB, and 1.24dB, respectively, and the axial ratio 3dB bandwidths are 0.33%,

0.08%, and 0.26%, respectively. The AWS band axial ratio can be improved by adjusting the relative dimensions of the AWS extensions. The antenna radiates with the desired polarizations in each configuration. Measured gain and axial ratio for each configuration are shown in Figures 4.10–4.12. Radiation patterns of the antenna at resonance are shown in Figure 4.13.

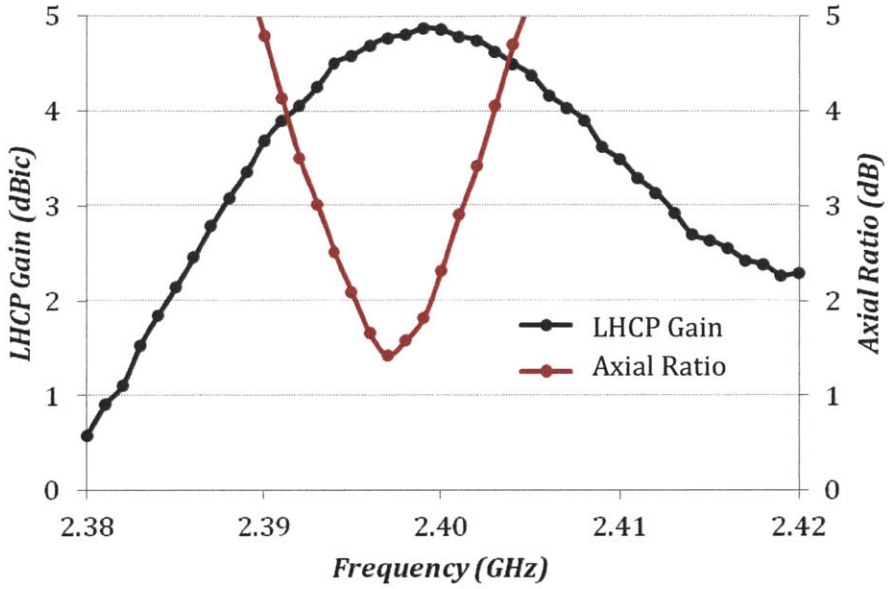

Figure 4.11: Measured peak LHCP gain and boresight axial ratio for ISM configuration

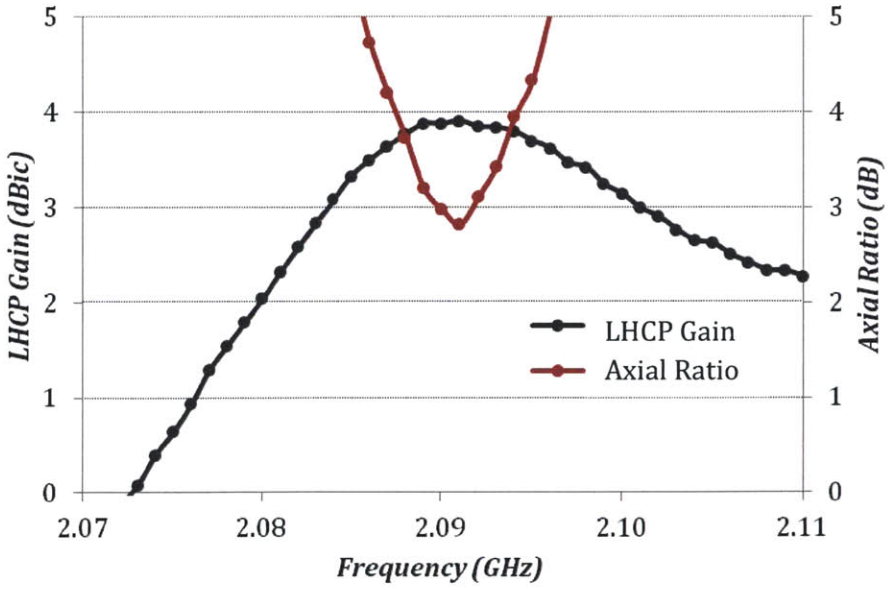

Figure 4.12: Measured peak LHCP gain and boresight axial ratio for AWS configuration

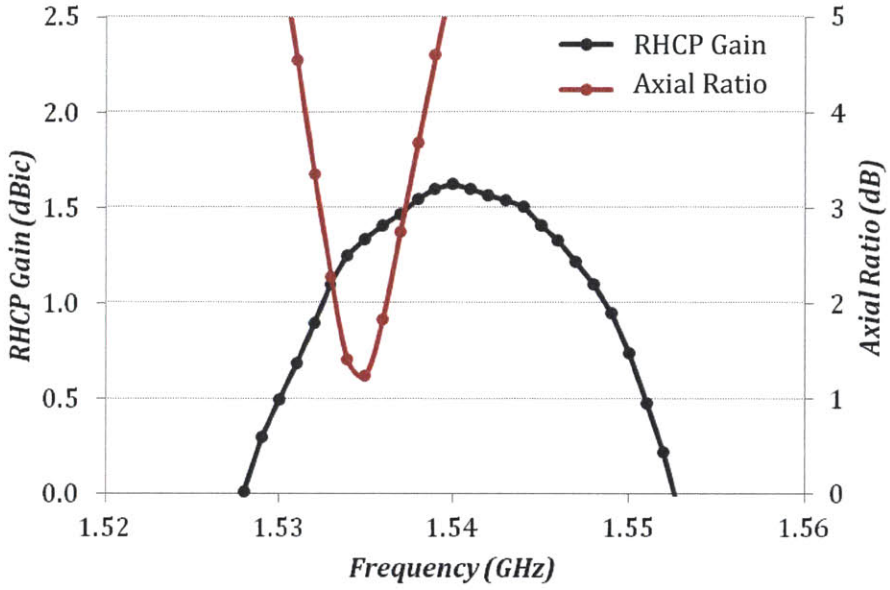

Figure 4.14: Measured peak RHCP gain and boresight axial ratio for GPS configuration

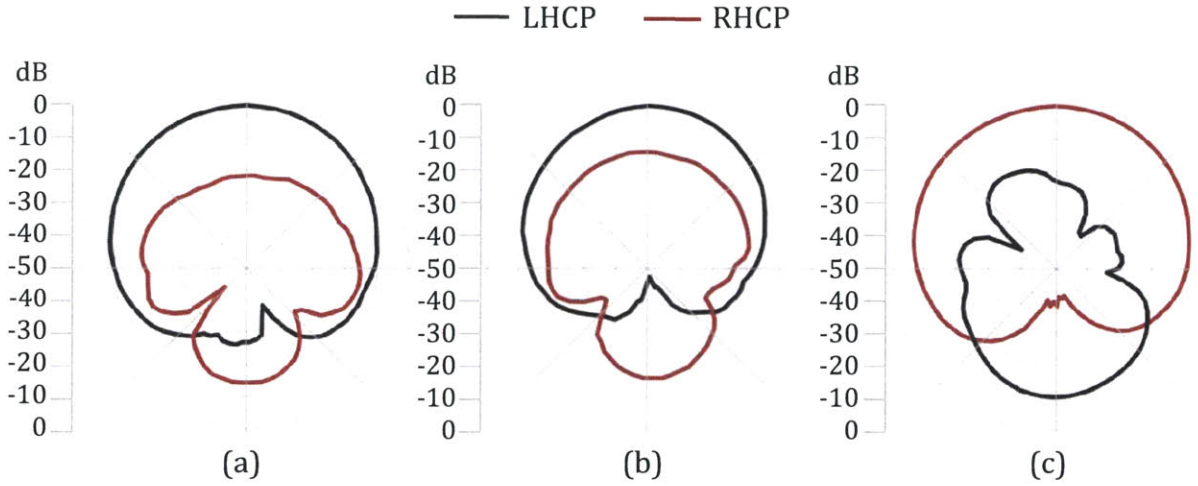

Figure 4.13: Normalized measured left and right hand circularly polarized radiation patterns for (a) ISM, (b) AWS, and (c) GPS configurations

A solid electrode cover was placed on top of the constructed antenna prototype to characterize the effect of the electrodes on the antenna's RF performance. No change was observed in the return loss of the antenna either in frequency or magnitude. Radiation pattern, polarization sense, and gain were essentially unaffected, with measured ISM gain actually increasing by 0.23dBic at boresight. AWS LHCP gain decreased by a mere 0.2dBic. GPS RHCP gain also increased by 0.04dBic. Comparative normalized radiation patterns are shown in Figure 4.14. Axial ratios for ISM, AWS, and GPS bands were also essentially unaffected, with net changes less than 0.25dB for all three bands and no change in polarization sense. One may note that the patterns shown in Figure 4.14 are not direct matches of those in Figure 4.13. This is likely due to rotation in tilt angle of the antenna for different measurements.

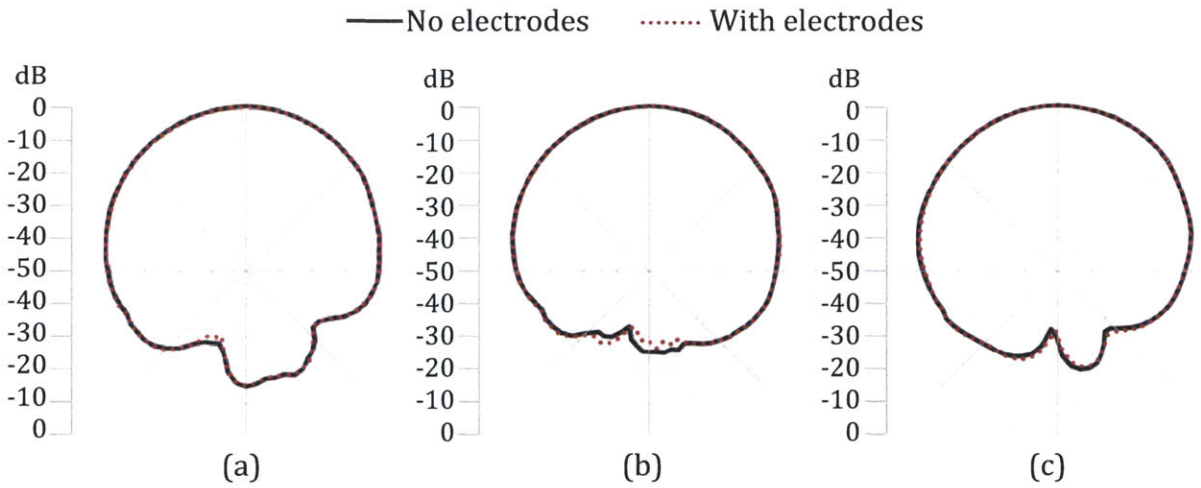

Figure 4.15: Normalized radiation patterns for co-polarizations with and without electrode cover for (a) ISM, (b) AWS, and (c) GPS configurations

4.6 Summary

The design of a compact three band frequency and polarization reconfigurable single-feed circularly polarized patch antenna using liquid metal microswitches has been presented. Reconfigurable operation was achieved by selectively connecting a central truncated corner patch antenna to sets of extensions using 16 of the electrostatic microswitches presented in Chapter 3. A liquid electrode method was used in the successful actuation of constructed prototypes. Measured results met the specified design objectives, achieving successful actuation, circular polarization, and desired gain and polarization sense in three switchable bands. A summarized comparison of objectives, simulated results, and measured results is presented in Table 4.2.

Measured operating frequencies are about 2% lower than designed for all three bands, which suggests that the designated dimensions can be simply scaled down to achieve the exactly desired frequencies. Although the AWS band axial ratio met specified minimums, the axial ratio can be improved in future designs by resizing the relative dimensions of the AWS extensions. Measured gain for the GPS band also meets minimum specifications but is lower than expected by about 2dBic. This might be a result of higher than expected resistance in some of the microswitches. Unfortunately, the antenna traces are not open for resistance testing due to the fluidic layer, and the lower than expected gain should be investigated in future work.

Initial characterization of the effect of solid electrodes on antenna performance indicates that the electrodes have minimal effect on the frequency of operation, gain, or axial ratio. The cover was designed to be symmetrical in order to minimize the effect of the cover on net polarization of the antenna. Future integratable versions of the antenna featuring a solid electrode network should not require significant modifications to the antenna geometry in order to compensate for the parasitic effects of the electrode network.

Table 4.2: Summary of antenna objectives, simulated results, and measured results

	Objectives	Simulated	Measured	✓ ✗
Frequency Agility	3 bands: ISM, AWS, GPS	3 bands: ISM, AWS, GPS	3 bands: ISM, AWS, GPS	✓
Polarization Agility	LHCP, LHCP, RHCP	LHCP, LHCP, RHCP	LHCP, LHCP, RHCP	✓
Boresight Gain	None	5.5dBic, 4.6dBic, 4.1dBic	4.9dBic, 3.9dBic, 1.6dBic	-
80° Elevation Gain	>-6.4dBic	-4.2dBic, -4.8dBic,-3.9dBic	-4.2dBic, -5.0dBic, -5.8dBic	✓
Impedance Bandwidth	None	16MHz, 27MHz, 19MHz	10MHz, 26MHz, 12.5MHz	-
Axial Ratio	≤3dB	1.43dB, 3.8dB, 0.61dB	1.43dB, 2.82dB, 1.37dB	✓
Axial Ratio Bandwidth	None	Not simulated*	7.9MHz, 1.7MHz, 4.0MHz	-
Footprint	≤10.25cm^2	10.24cm^2	10.24cm^2	✓
Thickness	≤110mils	84.5mils	85mils	✓
Mercury Content	≤15mg	14.13mg	13.88mg	✓
Comments	* Axial ratio bandwidths not simulated due to large memory allocation required.			

Chapter 5

Conclusions and Future Work

5.1 Summary

A novel method for antenna reconfiguration using electrostatic liquid metal microswitches has been presented and demonstrated on a three band frequency and polarization reconfigurable patch antenna. The proposed microswitches offer a linear, low resistance reconfiguration mechanism for applications that require minimal loss and maximization of structural area at slow switching speeds. Actuation was successfully demonstrated using an electrostatic liquid electrode method to manually open and close microswitches. Droplet movement was also induced using a solid electrode version of the microswitch that offers the possibility of a future integrated switch. These electrostatic switch designs have been shown to compare favorably against purely microfluidic designs.

The topology of the antenna presented as an application for the proposed microswitches is another contribution of this thesis. A clarified method for determination of polarization sense was used to design polarization agility as well as frequency agility into a single-feed circularly polarized reconfigurable patch. The antenna design benefited from the low resistances and out-of-plane control networks of the proposed microswitches to simplify a design with challenging radiation performance goals. Antenna frequency and polarization agility were successfully demonstrated using microswitches actuated with the liquid electrode method. The parasitic effect of a solid electrode control network on the antenna cover has been shown to be minimal, suggesting that an integrated solution is readily attainable with the current antenna design.

5.2 For Further Investigation

A number of research topics based directly upon the work presented in this thesis should be explored, including fabrication, optimization of the solid electrode method, integration, failure analysis of the proposed switches during dynamic operation, and wide bandwidth antenna feeding techniques.

Fabrication represents the foremost of these topics because the limits imposed by the current process are directly related to many of the other areas that require further investigation. Specifically, a process that allows for a thinner, higher permittivity dielectric film would lower minimum actuation voltage and result in more robust operation with either liquid or solid electrode techniques. Actuation would also be improved by

developing a process for smoother side walls for the switch slot, which should reduce friction within the switch. The application of a planarization layer to remove the step at the gap between solid metal traces would also reduce friction in the switch. The solid electrode covers could also benefit from an upgraded fabrication process that can minimize the gap between electrodes. This will reduce the chance that a droplet will actuate under one electrode and not experience sufficient field strength from a subsequently actuated adjacent electrode to reliably actuate. Many of these fabrication issues are eminently solvable with readily available cleanroom technologies, and the limits reached in this thesis are almost entirely circumstantial.

The optimization of the solid electrode method and achieving an integrated solution are closely tied to each other and to an improved fabrication process. The solid electrode method appears to be the ideal method for integration, but the technique requires precise control of device dimensions to ensure reliable two-way actuation. Unfortunately, reliable actuation can only be determined experimentally, and the verification of any improved design will likely require a number of prototype construction runs. Again, integration will benefit from improved processing techniques to lower required actuating voltage, which will reduce the transformer size requirements for practical wireless applications.

The lower than expected performance of the presented antenna at the GPS band also presents an opportunity for future work. The GPS configuration gain was lower than simulated by about 2.5dBic and lower than the gain of a hardwired version of the antenna by about 1.3dBic. Unfortunately, resistance measurements cannot be taken on the constructed antenna prototypes due to the fluidic layer that covers the entire antenna surface with the exception of the switch slots. Dynamic testing of the electrostatic switches should be performed to determine whether deleterious effects occur with repeated switching or whether resistance varies significantly across many switch cycles.

Lastly, the antenna design can be improved by using a wider band feeding technique. While convenient, the coaxial antenna feed is a narrow band technique, which can limit the usefulness of the antenna in many applications. Wide band methods such as proximity, aperture, or meandered probe feeds may improve the impedance bandwidths of each configuration of the antenna and provide a better impedance match across all three bands for a given feed location. Such feeds could also reduce sensitivity of the design to manufacturing tolerances, easing attainment of axial ratio and axial ratio bandwidth goals.

5.3 Future Directions

Although designed with patch antenna applications in mind, the electrostatic microswitches presented in this thesis are not limited to patches or antennas generally. In fact, the proposed microswitches may be suitable for any number of distributed RF

structures such as transmission line filters and matching networks. In these applications, mercury droplets may not necessarily be actuated only as switches, but can also be used as conductive elements with a continuously variable position. The suitability of such devices will be application-dependent. Mercury droplet devices are expected to be most useful in low speed tuning, product prototyping, or high power applications.

The proposed microswitches and liquid metal droplet manipulation methods presented in this thesis represent only a fraction of the potential for liquid metal devices in RF technology. Beyond switching and even flexible material applications, liquid metals offer the best chance for agility and reconfigurability in RF design through free form structures. A major limitation of any switching scheme regardless of the switch technology is that the number of configurations is very finite. Even though the proposed reconfigurable antenna achieves multiple modes of operation, those modes are ultimately set by the layout of the solid antenna structures, which are fixed. The switches simply select the activated mode. This is true even of massively switched designs such as pixilated antenna arrays, which simply scale down the solid metal structures in exchange for more switches.

True flexibility can be achieved when solid metal structures are completely replaced by liquid metals. If droplets of liquid metal can be manipulated reliably and locally contained by small structures that allow for droplet merging and splitting, a truly free form reconfigurable RF device may be within reach. Containment structures such as Laplace barriers [32] have already been demonstrated, and a form of liquid metal droplet manipulation has been demonstrated in this thesis. Devices merging these two concepts could be useful in prototyping applications and in the most demanding reconfiguration environments; changing from antennas to filters to transmission lines again and again. It is hoped that this work will aid such an achievement in the near future.

List of Figures

List of Tables

Bibliography

[1] RFMD, "RF MEMS switch technology for radio front end applications," http://www.rfmd.com/cs/documents/CommJCostaRWS10Presentation.pdf

[2] J.T. Bernhard, *Reconfigurable Antennas*. San Francisco, CA: Morgan & Claypool, 2007.

[3] D. Goldman, "Sorry, America: your wireless airwaves are full," http://money.cnn.com/2012/02/21/technology/spectrum_crunch/index.htm

[4] R. Rubenstein, "Radios get smart," http://spectrum.ieee.org/consumer-electronics/standards/radios-get-smart/1

[5] CTIA, *Semi-Annual Year-End 2012 Top-Line Survey Results*, http://www.ctia.org/advocacy/research/index.cfm/AID/10316

[6] S. Yong, "Design and analysis of pattern null reconfigurable antennas," Ph.D. dissertation, University of Illinois, Urbana, Jan. 2012.

[7] R. Leschhorn and K. Pensel, "Software radios for maximum flexibility and interoperability," in *Proceedings of Research and Technology Organization System Concepts and Integration Panel Symposium*, Oct. 2000.

[8] C. Balanis, *Antenna Theory: Analysis and Design*, 3rd ed., Wiley Interscience, New York, 2005.

[9] A. King, "A frequency reconfigurable slot antenna with a conductive microfluidic switching mechanism," M.S. thesis, Dept. Elec. and Comp. Eng., Univ. of Illinois at Urbana-Champaign, Champaign, IL, 2012.

[10] S. Mazlouman, X. Jiang, A. Mahanfar, C. Menon, and R. Vaughan, "A reconfigurable patch antenna using liquid metal embedded in a silicone substrate," in *IEEE Transactions on Antennas and Propagation*, vol. 59, pp. 4406—4412, July 2011.

[11] J. Langer, J. Zou, C. Liu, and J.T. Bernhard, "Reconfigurable out-of-plane microstrip patch antenna using MEMS plastic deformation magnetic actuation," *IEEE Microwave and Wireless Components Letters*, vol. 13, pp. 120—122, Mar. 2003.

[12] Microsemi, "Micronotes: Series 701-PIN Diodes," http://www.microsemi.com/design-support/application-notes#rf-and-pin-diodes

[13] Hewlett Packard, "Fast Switching PIN Diodes: Application Note 929," http://www.qsl.net/n9zia/wireless/pdf/an929.pdf

[14] Tawk, Y.; Hemmady, S.; Christodoulou, C.G.; Balakrishnan, G., "Measuring the transition switching speed of a semiconductor-based photoconductive switch using RF techniques," *Antennas and Propagation (APSURSI), 2011 IEEE International Symposium on* , vol., no., pp.972,975, 3-8 July 2011.

[15] Hansheng Su; Shoaib, I.; Xiadong Chen; Kreouzis, T., "Optically tuned polarisation reconfigurable antenna," *Antennas and Propagation (APCAP), 2012 IEEE Asia-Pacific Conference on* , vol., no., pp.265,266, 27-29 Aug. 2012.

[16] Panagamuwa, C.J.; Chauraya, A.; Vardaxoglou, J.C., "Frequency and beam reconfigurable antenna using photoconducting switches," *Antennas and Propagation, IEEE Transactions on* , vol.54, no.2, pp.449,454, Feb. 2006.

[17] Rebeiz, G.M. "RF MEMS Switches: Status of the Technology," http://www-mtl.mit.edu/researchgroups/mems-salon/xueen_rebeiz_03.pdf

[18] Sen, P.; Chang-Jin Kim, "Microscale Liquid-Metal Switches—A Review," *Industrial Electronics, IEEE Transactions on* , vol.56, no.4, pp.1314,1330, April 2009.

[19] Energy Star, (2010, November), *Information on compact fluorescent light bulbs (CFLs) and mercury* [Online]. http://www.energystar.gov/ia/partners/promotions/change_light/downloads/Fact_Sheet_Mercury.pdf

[20] S. Saffer, J. Simon, and C.-J. Kim, "Mercury-contact switching with gap closing microcantilever," in Proc. Micromachined Devices Compon. II, Austin, TX, Oct. 1996, pp. 204–209.

[21] J. Simon, S. Saffer, F. Sherman, and C.-J. Kim, "Lateral polysilicon microrelays with a mercury microdrop contact," IEEE Trans. Ind. Electron., vol. 45, no. 6, pp. 854–860, Dec. 1998.

[22] Y. Kondoh, T. Takenaka, T. Hidaka, G. Tejima, Y. Kaneko, and M. Saitoh, "High-reliability, high-performance RF micromachined switch using liquid metal," J. Microelectromech. Syst., vol. 14, no. 2, pp. 214–220, Apr. 2005.

[23] L. Latorre, J. Kim, J. Lee, P.-P. de Guzman, H. J. Lee, P. Nouet, and C.-J. Kim, "Electrostatic actuation of microscale liquid-metal droplets," *J. Microelectromech. Syst.*, vol. 11, no. 4, pp. 302–308, Aug. 2002.

[24] P. Sen and C.-J. Kim, "A fast liquid-metal droplet switch using EWOD," in *Proc. IEEE 20th Int. Conf. MEMS*, Kobe, Japan, 2007, pp. 767–770.

[25] M. Rashed Khan, G. J. Hayes, J.-H. So, G. Lazzi, and M. D. Dickey, "A frequency shifting liquid metal antenna with pressure responsiveness,"*Applied Physics Letters*, vol. 99, no. 1, pp. 1-3, July 2011.

[26] M. Kernaghan, "Surface tension of mercury," *Phys. Rev.*, vol. 37, no. 8, pp. 990-997, April 1931.

[27] L. Latorre, J. Kim, J. Lee, P.-P. de Guzman, H. Lee, P. Nouet, C.-J. Kim, "Electrostatic actuation of microscale liquid-metal droplets," *Journal of Microelectromechanical Systems*, vol. 11, no. 4, August 2002.

[28] Kai-Cheng Chuang and Shih-Kang Fan, "Direct Handwriting Manipulation of Droplets by Self-Aligned Mirror-Ewod Across a Dielectric Sheet," *Micro Electro Mechanical Systems, 2006. MEMS 2006 Istanbul. 19th IEEE International Conference on* , vol., no., pp. 538-541, 2006.

[29] F. Mugele and Jean-Chrstophe Baret, "Electrowetting: from basics to applications," *Journal of Physics: Condensed Matter*, vol. 17, no. 28, pp. R705, July 2005.

[30] H. Moon, S.K. Cho, R. Garrell, and C.-J. Kim, "Low voltage electrowetting-on-dielectric," *Journal of Applied Physics*, vol. 92, no. 7, pp. 4080–4087, Oct. 2002.

[31] K. Choi, A. Ng, R. Fobel, and A. Wheeler, "Digital microfluidics," *Annual Review of Analytical Chemistry*, vol. 5, pp. 413–440, Apr. 2012.

[32] E. Kreit, B.M. Mognetti, J.M. Yeomans, and J. Heikenfeld, " Partial-post laplace barriers for virtual confinement, stable displacement, and >5cm s^{-1} electrowetting transport," *Lab on a Chip*, vol. 11, pp. 4221-4227, Oct. 2011.